Citation: Cai, B., Xu, L., Wang, L. & Fu, F. (2025). Residual mechanical properties of steel-fibre-reinforced concrete with volcanic scoria sand after freeze–thaw cycles using machine learning. Proceedings of the Institution of Civil Engineers - Structures and Buildings, 178(10), pp. 878-900. doi: 10.1680/jstbu.25.00010

This is the accepted version of the paper.

This version of the publication may differ from the final published version.

Residual mechanical properties of steel-fibre-reinforced concrete with volcanic scoria sand after freeze–thaw cycles using machine learning

Bin Cai[1], Li Xu[1], Lin Wang[2] and Feng Fu[3*]

Bin Cai PhD
Professor, School of Civil Engineering, Jilin Jianzhu University, Changchun, Jilin, PR China
Li Xu BSc
Master's student, School of Civil Engineering, Jilin Jianzhu University, Changchun, Jilin, PR China
Lin Wang PhD
Associate Professor, School of Economics and Management, Jilin Jianzhu University, Changchun, Jilin, PR China
Feng Fu PhD, MBA, FICE
Senior Lecturer, Department of Engineering, School of Science and Technology, City, University of London, London, UK (corresponding author: feng.fu.1@city.ac.uk)

Abstract

In cold regions, using steel fibers (SF) and manufactured volcanic scoria sand (MVSS) for fiber-reinforced concrete formulation can mitigate the problem of deterioration of mechanical properties due to freeze-thaw (F-T) cycles and effectively reduces the consumption of natural sand (NS). To better predict the residual mechanical properties (RMP) of concrete after F-T cycles, this study develops four machine learning (ML) models: BPNN, CNN, DT, and CatBoost. The input variables were water/cement ratio (w/c), manufactured volcanic scoria sand replacement rate (RMVSS), steel fiber volume content (SFVC), and F-T cycles. The output values were compressive strength (CS) and splitting tensile strength (STS). Key indicators showed all models exhibited acceptable accuracy. CatBoost outperformed the other methods with RMSE of 0.391 and 0.037, MAE of 0.273 and 0.026, MAPE of 0.009 and 0.011, SI of 0.011 and 0.014, and IA of 0.999 and 0.999 for CS and STS, respectively. R^2 are all as high as 0.99. CatBoost shows the highest prediction accuracy. Sensitivity testing of the strength of steel fiber reinforced manufactured volcanic scoria sand concrete (SFMVSSC) using CatBoost and it showed F-T cycles were an essential parameter. Finally, scanning electron microscope (SEM) shows SF and MVSS can improve the frost resistance of concrete.

Keywords: Volcanic scoria; Fiber-reinforced concrete; Machine learning; Freeze-thaw; Mechanical properties

1. Introduction

Natural sand (NS) is a primary raw material for concrete production and positively affects concrete performance (Kang et al., 2023). The growth of building infrastructure in developing nations and the rehabilitation of existing infrastructure in developed countries has resulted in a global demand for sand that is projected to exceed 8 billion tons per year. This has led to a shortage of sand and gravel (Luo et al., 2023). In light of the imperative for sustainable development of natural resources and environmental protection, contemporary society is increasingly focused on the identification of substitute materials for construction (Benahsina et al., 2023; El-Nadoury et al., 2021). The utilisation of MVSS in lieu of NS for the design of concrete mixes is emerging as a pivotal aspect of the ecological development of construction materials across a range of countries. MVSS is widely used in northeast China and is rich in aggregate resources. In Huinan County alone, Jilin Province, China, there are 800 million m^3 of MVSS (Cai et al., 2021; Yang et al., 2017). The lightweight aggregate as MVSS aggregate has a structure resembling bubbles, porosity, lightweight, high refractoriness, low modulus of elasticity, strong water absorption, excellent resistance to frost and corrosion, robustness, and effective thermal insulation (Huang et al., 2023; Tchamdjou et al., 2017; Tchamdjou et al., 2017; Warati et al., 2019), but the higher brittleness of manufactured volcanic scoria sand concrete (MVSSC) limits the applicability of concrete compared with normal concrete (Li et al., 2019; Zhou et al., 2016).

Meanwhile, in cold regions or cold seasonal climates, concrete structures are inevitably exposed to F-T cycles (Liao et al., 2024; Dong et al., 2021; Bai et al., 2022), causing safety risks and economic losses, especially in northeastern China. Damage to concrete structures due to F-T cycles has attracted much attention. It is crucial to improve its mechanical properties and crack resistance after being subjected to F-T cycles (Li et al., 2022). Thus, fiber insertion can significantly reduce the brittleness and frost damage of concrete in cold or low-temperature regions. Due of its superior tensile strength, high elastic modulus, and resistance to cracks, SF is frequently utilized in construction projects where F-T damage might occur in cold climates (Xiao et al., 2018). SF can transform damage to the MVSSC matrix from abrupt brittle damage to predictable ductile damage, offering an early warning system for structural damage and absorbing part of the stresses in crossing cracks (Zhang et al., 2015; Zhang et al., 2024). Furthermore, SF lessens concrete permeability, enhances F-T resistance, and aids in reducing spalling, which is the crushing and cracking of concrete surfaces brought on by water saturation or F-T cycles (Pal et al., 2023; Karahan et al., 2011). Prior research has demonstrated that SF can prevent the growth of matrix cracks and considerably improve the performance of concrete in cold regions.

Accurate assessment of the RMP of SFMVSSC after F-T cycles is vital to ensure the safety and durability of concrete structures in cold regions. Although traditional testing methods can directly determine the change in mechanical properties of concrete after specific F-T conditions, these methods are often time-consuming and costly, and they are difficult to fully reflect the various material combinations and environmental conditions that may be encountered in actual projects (Liu et al., 2021). Over the past few decades, the application of ML or artificial intelligence (AI) in civil and structural engineering has grown due to ML advancements, making predicting the CS of concrete with great precision possible. ML models can facilitate the generation of reliable and accurate predictions from optimized design data, thereby reducing the expenditure of time, financial resources, and physical effort (Alarfaj et al., 2024; Tang et al., 2023). Over the years, various ML methods have been used to predict multiple material or concrete parameters, including artificial neural network (ANN), decision tree (DT), and random forest (RF). ANN is one of the most often used ML techniques for accurately predicting concrete CS (Maherian et al., 2023; Sun et al., 2023; Kioumarsi et al., 2023; Bouras et al., 2023; Hussain et al., 2022； Morsy et al., 2022; Laouissi et al., 2022). Back propagation neural network (BPNN) and convolutional neural network (CNN) are the most widely used ANN. BPNN has the advantage of being robust, but the model converges slowly and tends to get trapped in local minima. CNN, which was developed later, uses local connections and weight splitting to reduce the complexity of the model by exploring the relationship between input and output. Nevertheless, a substantial quantity of data is necessary for this process. The ANN algorithm also necessitates methods that have been tried and tested numerous times over an extended period to ascertain the ideal network properties, such as the number of neurons and hidden layers (Rondinella et al., 2023).

Classification techniques and DT algorithms can address the limitations of ANN approaches. Using straightforward decision criteria, the DT algorithm is a supervised ML technique that creates tree models to address classification or regression issues (Yang et al., 2024). Algorithms based on DT are among the best algorithms because they can generate prediction models with high accuracy, stability, and ease of interpretation and represent nonlinear relationships well (Thai et al., 2023). Currently prevalent ensemble learning methods include Boosting, Bagging, and Stacking methods, which improve the generalization of the models in various ways and provide better results than independent traditional empirical models (Vadavalli et al., 2020; Zhang et al., 2012). Tran et al. predicted the CS of concrete with recycled aggregates using an XGBoost-based integrated learning framework and the traditional SVR model. According to the findings, the XGBoost model outperformed the conventional ML model (Quan et al., 2022). AdaBoost, Gradient Boost, CatBoost, and XGBoost were among the 13 ML models that Pal et al. employed to estimate the CS of fiber reinforced rubber recycled aggregate concrete; CatBoost proved to be the best accurate model (Pal et al., 2023). The CatBoost method is built on innovative feature processing algorithms that give strong prediction accuracy and computational efficiency priority, allowing it to outperform other notable gradient boosting competitors on various datasets (Candice et al., 2020). In summary, while ML algorithms are an evolving and progressive process, and ANN and DT-based models can accurately predict concrete strength, relatively few models are available that examine the SFMVSSC's mechanical characteristics following F-T cycles.

Based on this, this study aims to create ML models to forecast the RMP of SFMVSSC after F-T cycles. Three conventional single models (BPNN, CNN, DT) and an ensemble learning model (CatBoost) were employed to forecast the frost resistance of SFMVSSC. The w/c (0.4, 0.5), RMVSS (25, 50, 75%), SFVC (0, 0.5, 1, 1.5%), and F-T cycles (0, 50, 100, 150, 200 times) were used as input data. In contrast, CS and STS were used as output. The degree to which the RMP of SFMVSSC may be accurately predicted using the ML approach following F-T cycles is assessed by comparing the predictive outcomes of the model with the test findings. Additionally, the model's superiority is assessed. Finally, the damage mechanism of SFMVSSC following F-T cycling was examined using SEM. The experimental results and related analysis presented in this article can be a valuable guide for the practical application of SFMVSSC in extremely cold regions.

2. Experimental database

2.1 Materials

According to the Chinese standard JGJ51-2002 (CABR 2002), P • O42.5 ordinary silicate cement with a density of 3.1 kg/m^3 was selected to design the MVSSC used in the test. Crushed stone with a maximum grain size of 20 mm and a 1550 kg/m^3 density made up the coarse aggregate. Both NS and MVSS were combined to create the fine aggregate. SF (see Table 1 for physical properties) was mixed with the concrete as reinforcing material. In Fig.1, the materials are displayed. Table 2 displays the chemical makeup of MVSS. Table 3 and Fig. 2 display the physical characteristics and grading curves of the two types of sand, respectively.

Table 1. Physical properties of SF

Steel fiber	Length (mm)	Width (mm)	Thickness (mm)	Equivalent diameter (mm)	Aspect ratio	Density (g/cm^3)
CSF	38	1	0.35-0.5	0.76	50	7.8

Table 2. Chemical composition of MVSS

Chemical composition	SiO_2	Al_2O_3	TFe_2O_3	CaO	MgO	K_2O	Na_2O	TiO_2	P_2O_5	LOI	MnO
Content (%)	67.85	14.50	3.55	2.24	0.85	2.59	2.56	0.51	0.10	5.04	0.09

Table 3. Physical properties of sand

Materials	Bulk density (kg/m^3)	Apparent density (kg/m^3)	Porosity (%)	Clay content (%)
Natural sand	1424	2610	45.4	0.7
Scoria sand	1178	2360	50.0	1.1


Natural sand

Manufactured volcanic scoria sand

Gravel

Steel fiber

Fig. 1. Materials.

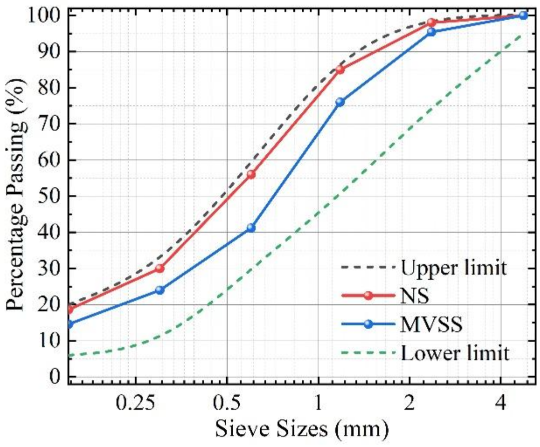

Fig. 2. Gradation curve of sand.

2.2 Mix Design

To further more about the frost resistance of SFMVSSC, a total of 24 different mix proportions were proposed based on three levels of RMVSS (25, 50, 75%), two w/c (0.4, 0.5), and four SFVC (0, 0.5, 1, 1.5%). Table 4 provides specific proportional information.

Table 4. Mix proportions for SFMVSSC

RMVSS	Cement	NS	Crushed	MVSS	SFVC (%)	w/c

	(kg/m³)	(kg/m³)	stone (kg/m³)	(kg/m³)		
25%	403.0	586.7	1155.6	159.1	[0-1.5]	0.4
50%	403.0	391.1	1155.6	317.9	[0-1.5]	0.4
75%	403.0	195.6	1155.6	476.9	[0-1.5]	0.4
25%	403.0	586.7	1155.6	159.1	[0-1.5]	0.5
50%	403.0	391.1	1155.6	317.9	[0-1.5]	0.5
75%	403.0	195.6	1155.6	476.9	[0-1.5]	0.5

2.3 Test setup

Test procedure: 1) Prepare 720 standard cubic test specimens with strength class LC40 by Chinese standard JG151-2002 (CABR 2002). Fig. 3 shows the process of test specimen fabrication. 2) Perform a F-T cycle test on specimens. The prepared specimens were placed in the F-T unit, as indicated in Fig. 4, and the F-T cycle test was conducted using the rapid freezing method outlined in the Chinese standard GB/T 50082-2009(CABR 2009). 3) The Chinese standard GB/T 50081-2019 (CABR 2019) was used to conduct STS and CS tests on the specimens that underwent the F-T cycle. The test diagrams are shown in Fig.5. The variations in the SFMVSSC specimens' microstructure during the F-T cycles were analyzed by SEM according to ASTM C1723-16 (ASTM 2016).

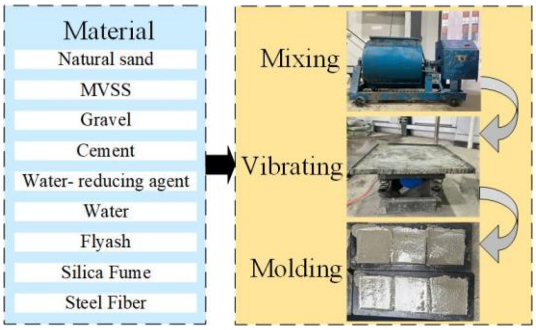

Fig. 3. Diagram illustrating the experimental process flow.

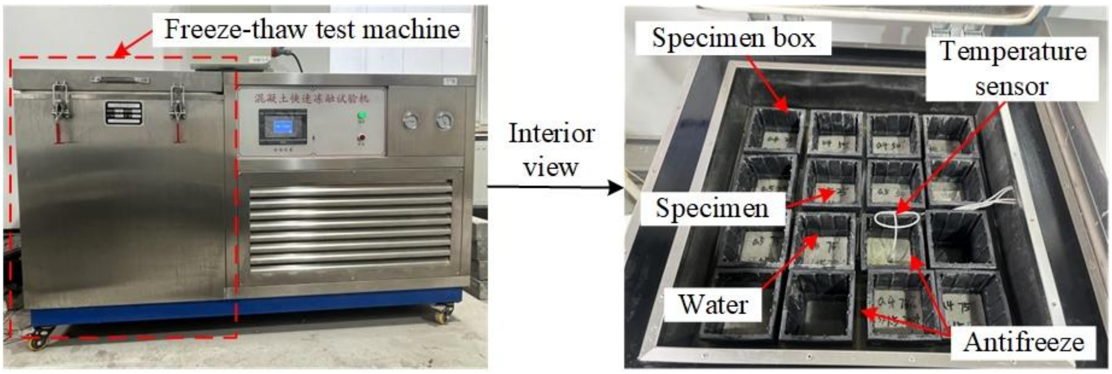

Fig. 4. F-T cycle test.

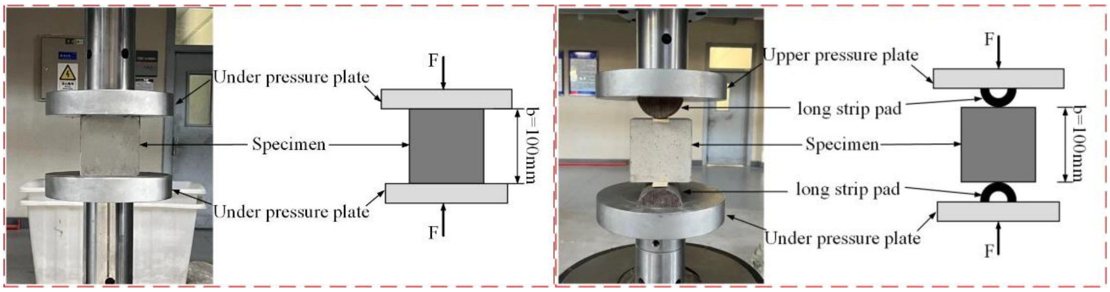

(a) **(b)**

Fig. 5. Strength test: (a)CS;(b) STS.

2.4 Experimental database

A total of 720 CS and STS specimens were tested, with an average of three specimens for each condition. This produced 240 sets of test data, 120 for CS and 120 for STS. The data input parameters are w/c, RMVSS, SFVC and F-T cycle. The output parameters are CS and STS. The CS and STS input and output parameters are shown in Table 5. The names, units, minimum and maximum values, mean and standard deviation (SD) of the input and output parameters are listed in Table 6.

Table 5. CS and STS input and output parameters.

No.	w/c	F-T cycle(times)	SFVC(%)	RMVSS(%)	CS(MPa)	STS(MPa)
1	0.4	0	0	25	43.891	3.651
2	0.4	50	0	25	40.953	3.268
3	0.4	100	0	25	38.036	2.911
4	0.4	150	0	25	30.130	2.370
5	0.4	200	0	25	25.980	2.041
6	0.4	0	0.5	25	44.970	3.790
7	0.4	50	0.5	25	41.962	3.392
8	0.4	100	0.5	25	38.973	3.023
9	0.4	150	0.5	25	30.872	2.461
10	0.4	200	0.5	25	26.620	2.119
11	0.4	0	1	25	46.419	3.986
12	0.4	50	1	25	43.314	3.568
13	0.4	100	1	25	40.228	3.180
14	0.4	150	1	25	31.866	2.589
15	0.4	200	1	25	27.477	2.230
16	0.4	0	1.5	25	46.910	4.080
17	0.4	50	1.5	25	43.770	3.652
18	0.4	100	1.5	25	40.652	3.254
19	0.4	150	1.5	25	32.202	2.650
20	0.4	200	1.5	25	27.767	2.828
-	-	-	-	-	-	-
-	-	-	-	-	-	-
-	-	-	-	-	-	-
-	-	-	-	-	-	-
-	-	-	-	-	-	-
116	0.5	0	1.5	75	36.718	3.113
117	0.5	50	1.5	75	32.615	2.830
118	0.5	100	1.5	75	29.222	2.508
119	0.5	150	1.5	75	25.353	2.091
120	0.5	200	1.5	75	22.118	1.800

Table 6. Summary of dataset for ML models.

Type	Parameters	Unit	Minimum	Maximum	Mean	SD
Input	w/c	/	0.4	0.5	0.45	0.050
Input	RMVSS	%	25	75	50	20.498
Input	SFVC	%	0	1.5	0.75	0.561
Input	F-T cycle	Times	0	200	100	71.007
Output	CS	MPa	20.651	46.91	32.684	6.712
Output	STS	MPa	1.619	4.08	2.676	0.591

Fig. 6 and Fig. 7 depict the basic linear fits of CS and STS with respect to each input characteristic, respectively. In this figure, R^2 is used to assess the accuracy of the fit. As can be seen in Fig. 6, the CS decreases with increasing w/c, RMVSS, and F-T cycles, and increases with increasing SFVC. The trend of STS with each input parameter is consistent with the CS (Fig. 7). As can be seen from Fig. 6 and Fig. 7, the relationship between strength and F-T cycles appeared to be a good linear fit with a high coefficient of determination R^2 of 0.779 (Fig. 6(d)) and 0.776 (Fig. 7(d)), respectively. Overall, the R^2 values of the simple linear fits were less than 0.8, and a more integrated approach is needed to improve the prediction accuracy.

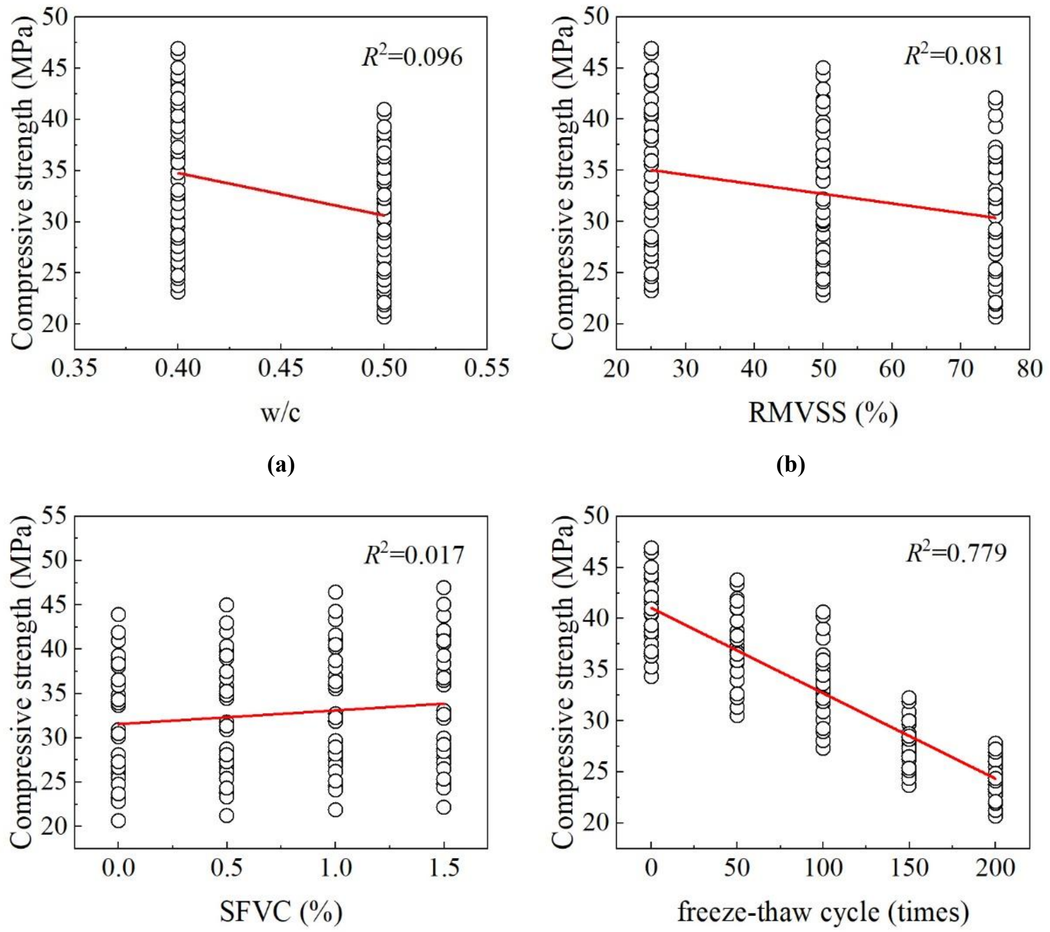

(a) **(b)**

(c) **(d)**

Fig. 6. Basic linear fit between CS and each input variable: (a) w/c; (b) RMVSS; (c) SFVC; (d) F-T cycle.

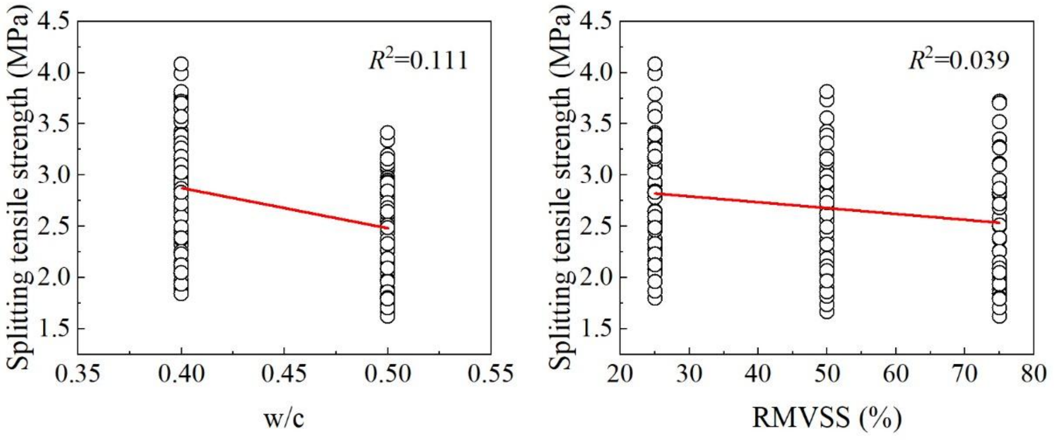

(a) **(b)**

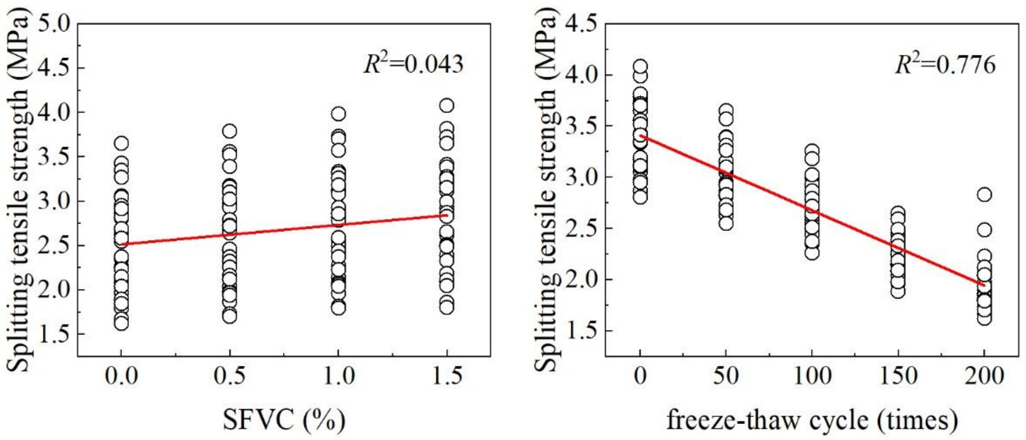

(c) **(d)**

Fig. 7. Basic linear fit between STS and each input variable: (a) w/c; (b) RMVSS; (c) SFVC; (d) F-T cycle.

Since some specific variables may be interdependent, correlation coefficients were determined for all possible variables, as shown in Fig. 8. An indicator of the strength of the association is its absolute value. In a correlation matrix, a correlation coefficient is a number between +1 and -1, where positive values denote a positive relationship between variables and negative values, the opposite of a relationship (Hussain et al., 2022), and the diagonal term is exactly one because the variable is always perfectly correlated with itself. Overly high correlation coefficients among input elements might result in inefficiencies and make it more difficult to comprehend how different aspects influence outcomes (Pal et al., 2023). According to the results, the independent input variables did not exhibit any significant link, and the experimental database was created using this data.

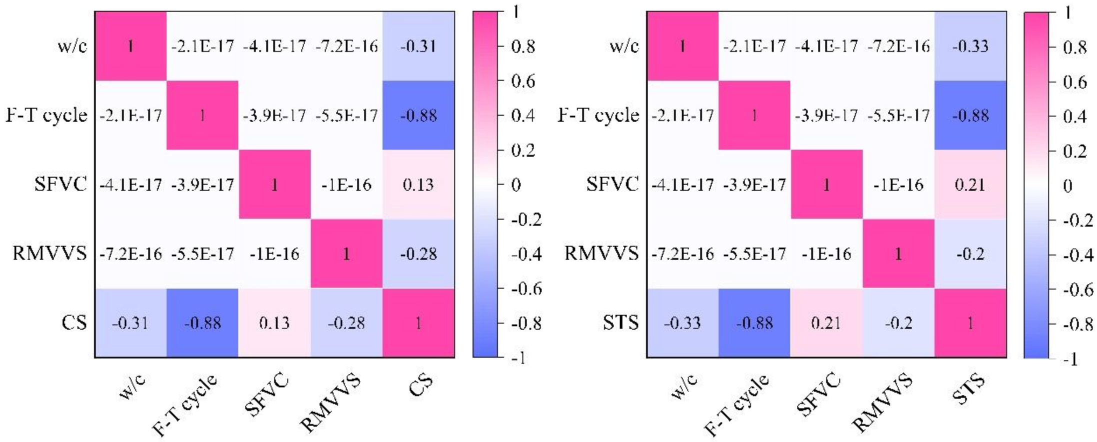

	w/c	F-T cycle	SFVC	RMVVS	CS
w/c	1	-2.1E-17	-4.1E-17	-7.2E-16	-0.31
F-T cycle	-2.1E-17	1	-3.9E-17	-5.5E-17	-0.88
SFVC	-4.1E-17	-3.9E-17	1	-1E-16	0.13
RMVVS	-7.2E-16	-5.5E-17	-1E-16	1	-0.28
CS	-0.31	-0.88	0.13	-0.28	1

	w/c	F-T cycle	SFVC	RMVVS	STS
w/c	1	-2.1E-17	-4.1E-17	-7.2E-16	-0.33
F-T cycle	-2.1E-17	1	-3.9E-17	-5.5E-17	-0.88
SFVC	-4.1E-17	-3.9E-17	1	-1E-16	0.21
RMVVS	-7.2E-16	-5.5E-17	-1E-16	1	-0.2
STS	-0.33	-0.88	0.21	-0.2	1

(a) **(b)**

Fig. 8. Correlation heat map: (a) CS;(b) STS.

3. Machine learning

Advanced computational algorithms and ML techniques are combined in AI in civil engineering to optimize construction processes, improve infrastructure design, and raise project efficiency and safety standards. As a subset of AI, ML can create predictive models from empirical data without thoroughly comprehending the underlying physical mechanisms. They are especially well-suited for forecasting material properties because of this feature, such as the CS of concrete, which is influenced by numerous factors (Maherian et al., 2023). This study used several ML models to predict the CS and STS of SFMVSSC after F-T cycles. A flow chart that depicts the research process is shown in Fig. 9.

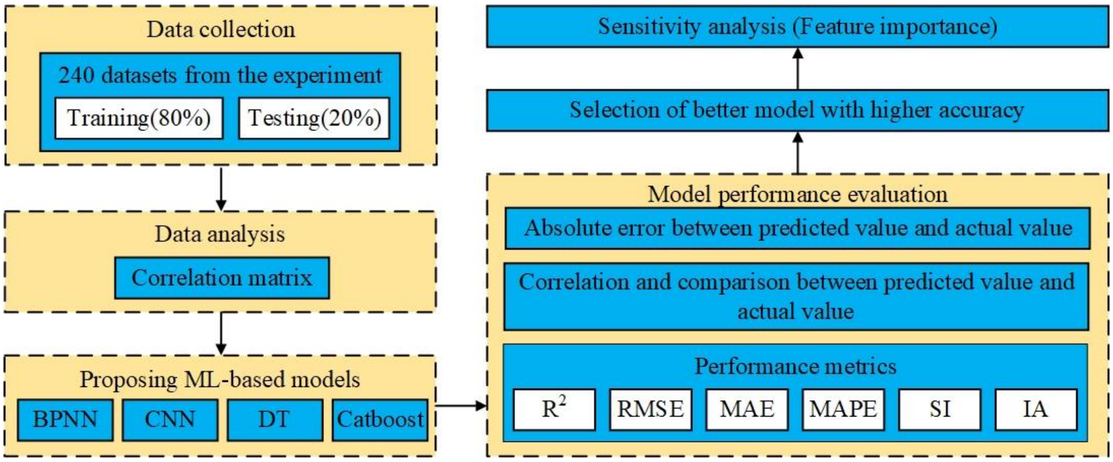

Fig. 9. Research scheme flowchart.

3.1 Decision tree (DT)

DT is an adaptable and easy-to-understand nonparametric supervised learning method for classification and regression problems (Mahmoudian et al., 2023). It has a hierarchical tree structure with root, branch, terminal and leaf nodes. By placing examples in a tree from the root to one or more leaf/end nodes—which designate the class of the instance—a DT groups instances into classes. Each node in the tree represents a test case for a specific attribute, and the edges that descend from each node define optional test case solutions. Depending on the split attribute, this recursive procedure is applied to each subtree whose root is at a new node. The cycle repeats until no more split attributes or all instances belong to the same class (Pal et al., 2023). The simplicity and ease of interpretation of DT make them a preferred option across various industries. DT takes into account the w/c, RMVSS, SFVC, and F-T cycles and does not set a maximum depth for the tree so that the tree grows until each leaf fewer than the minimum number of samples. A four-layer DT structure is schematized in Fig. 10.

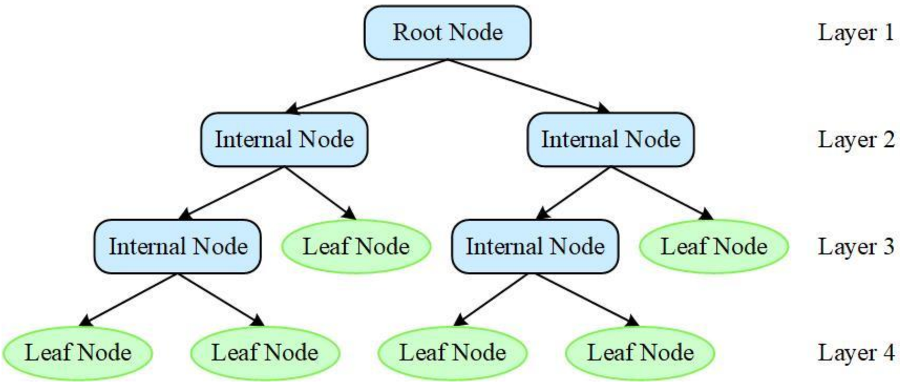

Fig. 10. DT structure.

3.2 Categorical gradient boosting (CatBoost)

The CatBoost algorithm is an algorithmic framework based on a DT with gradient boosting proposed by PROKHORENKOVAL et al. in 2017, a high-performance ML algorithm developed and improved using gradient boosting algorithms that outperform other leading gradient boosting competitors (Yang et al., 2024). Gradient boosting algorithms first compute the loss function of a weak ML algorithm (e.g., a DT) in the feature space and then build a strong ML algorithm model by reducing the value of the loss function by a weighted combination of weak ML algorithms and iterating continuously. Gradient boosting algorithms are a vital method for training algorithms with heterogeneous features and noisy data and solving complex dependency prediction problems. Fig. 11 shows the development of DT into CatBoost models, illustrating the history of tree-based model development. The CatBoost algorithm constructs a DT based on the gradient boosting algorithm. It uses preprocessing to handle categorical features during the training process. It utilizes the sort boosting strategy to solve the gradient bias and prediction bias problems existing in the gradient boosting algorithm while choosing the symmetric DT structure as the basic structure of the algorithm, calculating and controlling the number of leaf nodes to improve the speed of the constructed model and avoid over-fitting (Chang et al., 2023). CatBoost's schematic structure is displayed in Fig. 12.

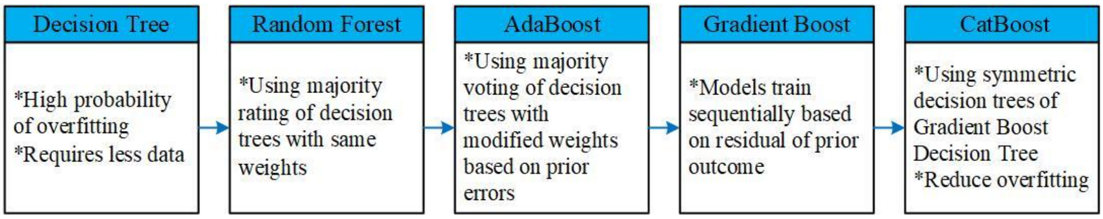

Fig. 11. Development history of tree-based models.

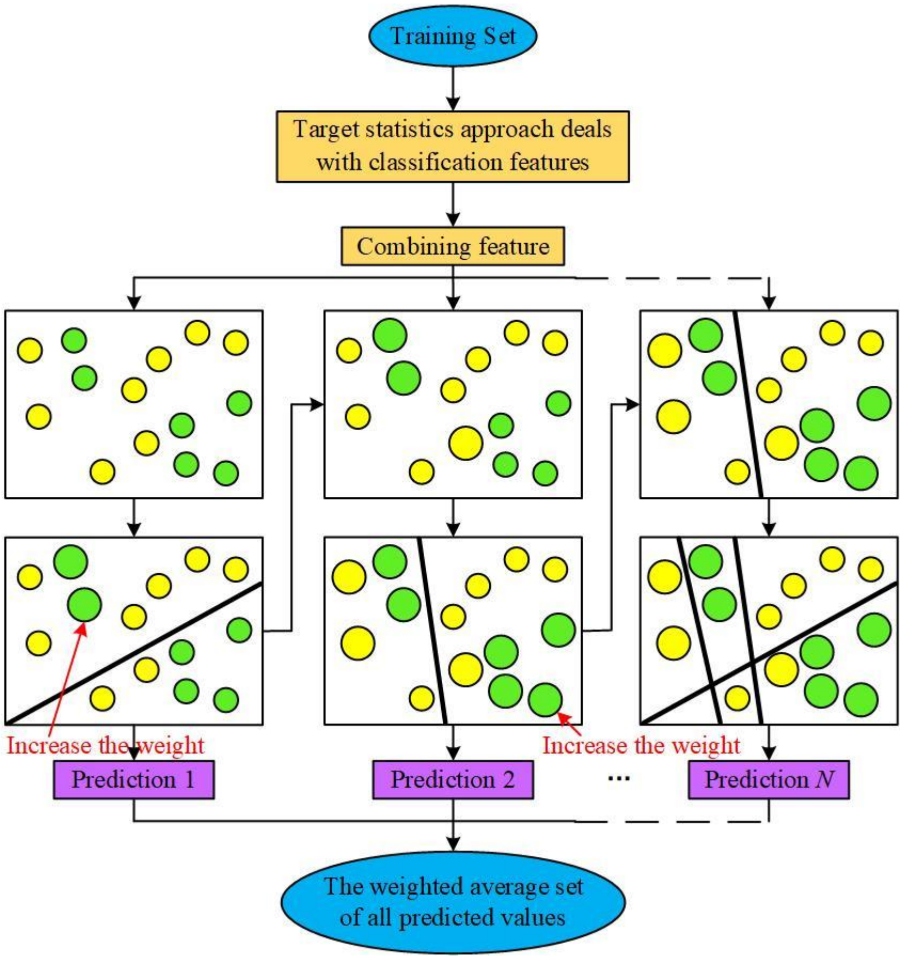

Fig. 12. CatBoost structure.

During CatBoost training, each iteration produces a weak learner, and eventually, a strong learner is acquired to minimize the model's overall loss function. The objective function, i.e., the parameters of the weak learner, for the *t* round of iteration is shown in eq. (1):

$$h_t = \arg\min El\left(y, F_{t-1}\left(x\right) + h_t\left(x\right)\right) \tag{1}$$

Where: E is the expectation function; y is the sample label; x is the input sample; F_{t-1} (x) is the first t-1 rounds of strong learners that already have training; $h_t(x)$ is the addition of new weak learners; l (y,F_{t-1}(x)) is the loss function of the first t-1 rounds of strong learners that already have training; l (y,F_{t-1}(x) +h_t(x)) is the sum of the loss functions of the first t-1 rounds of strong learners that already have training and the addition of new weak learners.

Since iterations are performed in the direction of the fastest descent of the loss function, the approximation of the loss in each round is represented by the negative gradient of the loss function, as in eq. (2):

$$-g_t\left(x, y\right) = -\frac{\partial\, l\left(y, F_{t-1}\left(x\right)\right)}{\partial\, F_{t-1}\left(x\right)} \tag{2}$$

Where: -g_t(x,y) is the negative gradient of the loss function.

The final strong learner for round t is obtained, see eq. (3):

$$F_t\left(x\right) = F_{t-1}\left(x\right) + l_{\mathrm{r}} h_t \tag{3}$$

Where: F_t (x) is the strong learner of round t; l_{r} is the learning rate for each iteration.

CatBoost uses w/c, RMVSS, SFVC, and F-T cycles as input data. The learning rate is a very important parameter, and the search interval is extended by the control variable method and combined with tenfold cross-validation to explore the best learning rate settings. The parameters of CatBoost are set as follows: the learning rate is 0.03, the tree depth is 6, the number of trees is 1,000, and the remaining parameters are adopted as default parameters.

In general, data must be preprocessed before entering the algorithm. A popular data preprocessing technique (Cai et al., 2022) that converts input and output data into the range [0,1] is data normalization, see eq. (4), used by all four ML algorithms. In all four ML techniques, the model is trained using 80% of the input data and validated using the remaining 20%.

$$X_{i,t} = \frac{X_i - X_{min}}{X_{max} - X_{min}} \tag{4}$$

Where $X_{i,t}$ is the input/output data, X_{min} and X_{max} represent the lowest and greatest values within the data fluctuation range, respectively.

3.3 ANN

The architecture and operation of neural networks in the human brain are simulated by the ANN (Alyaseen et al., 2024). Many artificial neurons with varying weight connections make up the ANN. The ANN can extract patterns and characteristics by learning from the input data. It uses them to solve classification, prediction and pattern recognition tasks with strong nonlinear mapping, generalization and fault tolerance (RodrÃ- guez-SÃ¡ nchez et al., 2024). Three layers make up a neural network: an input layer, an output layer, and one or more hidden layers, with one or more neurons in each layer connected to the next layer via weights to accommodate complex, nonlinear relationships. In the ANN model, the determination of the number of hidden layer nodes is very important, too few or too many hidden layer nodes can make the network unable to learn or overfitting. The number of hidden layers in the model is determined in eq. (5):

$$i = \sqrt{m+n} + a \tag{5}$$

Where: *i* is the number of hidden layer nodes; *m* is the number of input layer nodes; *n* is the number of output layer nodes; *a* is an integer between 0 ~ 10. Iterative training is carried out for models with different numbers of hidden layers, and then the number of model layers with optimal accuracy is used. After several calculations and training for the CS database, according to the results in Table 7, a comprehensive comparison of R^2, RMSE, MAE and MAPE reveals that the best training effect is found when the hidden layer is 6.

Table 7. Results for different nodes in the ANN hidden layer

Node number	R^2	RMSE	MAE	MAPE
2	0.885	2.417	1.901	0.062
3	0.871	2.550	1.896	0.064
4	0.881	2.449	1.851	0.053
5	0.887	2.283	1.879	0.058
6	0.890	2.362	1.838	0.053
7	0.865	2.611	2.092	0.061
8	0.889	2.374	1.723	0.055
9	0.885	2.306	1.985	0.060
10	0.884	2.301	1.874	0.059
11	0.877	2.495	1.969	0.061

BPNN and CNN are more widely used artificial neural networks (Zhang et al., 2020; Yu et al., 2022). Fig. 13 depicts the structure of the BPNN model, which has an input layer, six hidden layers, and an input layer. Fig. 14 illustrates the construction of the CNN model, which consists of an input layer, a convolution layer, a pooling layer, two fully connected layers (FC1, FC2), and an output layer. The input layers all consist of the w/c, RMVSS, SFVC, and F-T cycles. CS and STS are used as input layers.

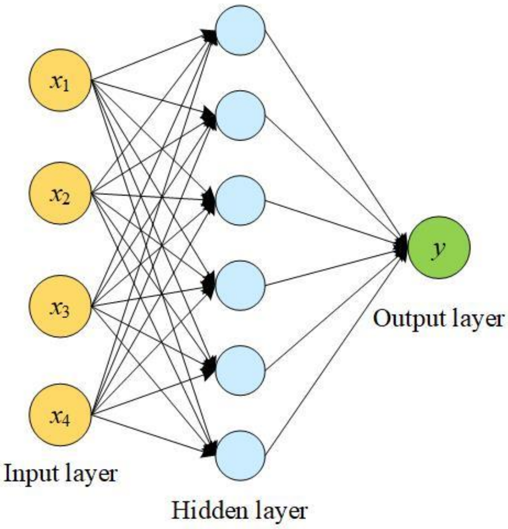

Fig. 13. BPNN structure.

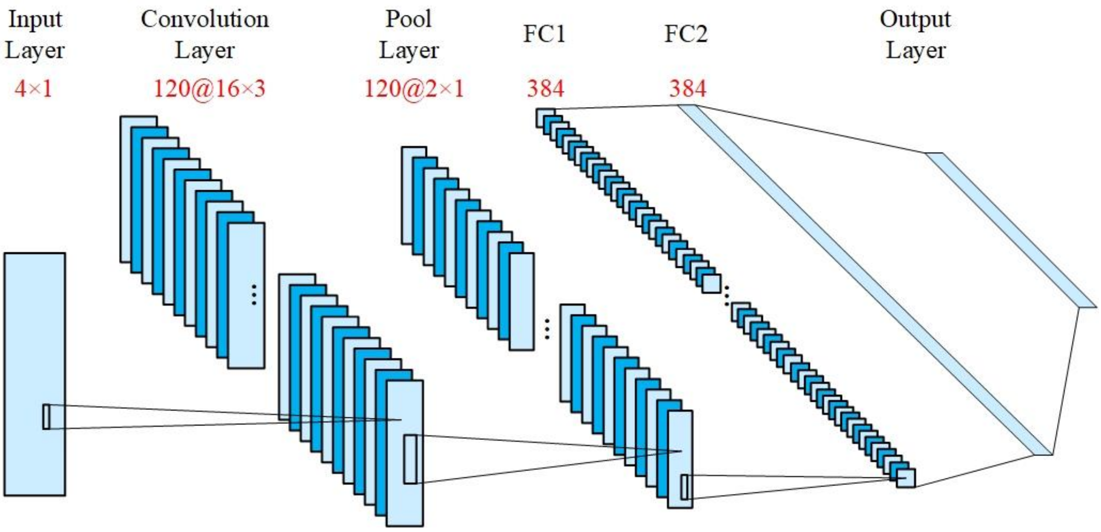

Fig. 14. CNN structure.

3.4 Model performance evaluation

The calculation of performance parameters is evaluated each model's performance. The following assessment criteria were applied to confirm the precision of ML models, including the coefficient of determination (R^2), root mean squared error (RMSE), mean absolute error (MAE), mean absolute percentage error (MAPE), scatter index (SI), and index of agreement (IA); the six indices are shown in eq. (6-11) (Sun et al., 2023):

$$R^2 = 1 - \frac{\sum_{i=1}^{n}\left(P_i - T_i\right)^2}{\sum_{i=1}^{n}\left(T_i - T\right)^2} \tag{6}$$

$$RMSE = \sqrt{\frac{\sum_{i=1}^{n}\left(P_i - T_i\right)^2}{n}} \tag{7}$$

$$MAE = \frac{\sum_{i=1}^{n}\left|P_i - T_i\right|}{n} \tag{8}$$

$$MAPE = \frac{\sum_{i=1}^{n}\left|\frac{P_i - T_i}{T_i}\right|}{n} \tag{9}$$

$$SI = \sqrt{\frac{\sum_{i=1}^{n}\left[\left(P_i - \frac{\sum_{i=1}^{n} P_i}{n}\right) - \left(T_i - \frac{\sum_{i=1}^{n} T_i}{n}\right)\right]^2}{\sum_{i=1}^{n} T_i^2}} \tag{10}$$

$$IA = 1 - \frac{\sum_{i=1}^{n}\left(P_i - T_i\right)^2}{\sum_{i=1}^{n}\left(\left|P_i - \frac{\sum_{i=1}^{n} P_i}{n}\right| + \left|T_i - \frac{\sum_{i=1}^{n} T_i}{n}\right|\right)^2} \tag{11}$$

Where n is the data set has a total of samples, P_i is the predicted sample value, T_i is the test sample value, and T is the average of all test values.

R^2, which varies from 0 to 1, shows how well the actual data is approximated. Greater values suggest that the regression model has a stronger explanatory capacity. Whereas MAE shows the mean error between actual and predicted values, RMSE quantifies the difference between actual and predicted values. MAPE can clearly explain the relative error. Generally, RMSE, MAPE, MAE, and SI values are lower for more accurate models. Conversely, a higher IA value corresponds to better model performance.

4. Results

Different methods can evaluate prediction models. This study assessed models using R^2 for the training and test sets and RMSE, MAE, MAPE, SI, and IA for the test set. By calculating the discrepancy between the actual and anticipated values, these metrics assess the prediction accuracy of models. Table 8 summarizes the performance metrics for each model. The RMSE for CS and STS is 2.362 and 0.177 for BPNN, 0.985 and 0.082 for CNN, 2.865 and 0.204 for DT, and 0.391 and 0.037 for CatBoost; for MAE, BPNN is 1.838 and 0.140, CNN is 0.771 and 0.074, DT is 2.403 and 0.165, and CatBoost is 0.273 and 0.026; and in MAPE, BPNN is 0.053 and 0.060, CNN is 0.026 and 0.030, DT is 0.074 and 0.068, and CatBoost is 0.009 and 0.011. The models with the best results should also have lower SI and higher IA values. The SI for CS and STS for BPNN is 0.069 and 0.065, CNN is 0.019 and 0.029, DT is 0.081 and 0.078 and CatBoost is 0.011 and 0.014; for IA, BPNN is 0.968 and 0.974, CNN is 0.995 and 0.995, DT is 0.954 and 0.960, and CatBoost is 0.999 and 0.999.

Table 8. Description of the performance measures for each model.

Prediction model		R^2		RMSE	MAE	MAPE	SI	IA	SD
		Training	Test						
BPNN	CS	0.953	0.890	2.362	1.838	0.053	0.069	0.968	6.334
	STS	0.921	0.905	0.177	0.140	0.060	0.065	0.974	0.552
CNN	CS	0.984	0.981	0.985	0.771	0.026	0.019	0.995	7.010
	STS	0.984	0.980	0.082	0.074	0.030	0.029	0.995	0.547
DT	CS	0.838	0.838	2.865	2.403	0.074	0.081	0.954	6.589
	STS	0.872	0.874	0.204	0.165	0.068	0.078	0.960	0.467
CatBoost	CS	0.999	0.997	0.391	0.273	0.009	0.011	0.999	6.965
	STS	0.999	0.996	0.037	0.026	0.011	0.014	0.999	0.560

5. Discussion

5.1 Model analysis

According to the analysis in Table 8, while all methods perform similarly, the CatBoost model has the lowest RMSE, MAE, MAPE, and SI, the highest IA, and the highest accuracy. Fig. 15 shows the comparison of the developed models in the form of a radar plot. In the radar plot, the overall performance of the models is reflected by the polygon area coverage, i.e., the smaller the area indicates the better the overall performance, and according to the Fig. 15, it can be found that CatBoost covers the smallest area, thus indicating the optimal performance of the CatBoost model. Avijit et al. also showed that CatBoost is a better-performing model (Pal et al., 2023). In the study of Avijit et al. the R^2 for training and test data of ANN was 0.896, 0.826 and R^2 for DT was 0.928, 0.786 respectively, while the R^2 for CatBoost was 0.934, 0.865 and R^2 for CatBoost was closest to 1. The RMSE, MAE and MAPE values of CatBoost are 6.632, 4.799 and 12.944 respectively, DT is 8.353, 5.662 and 15.104 respectively and ANN is 7.534, 5.563 and 18.639 respectively, which shows that CatBoost has the lowest RMSE, MAE and MAPE values. The results of this paper are consistent with the study of Avijit et al. The CatBoost model makes more accurate predictions about the RMP of SFMVSSC after F-T cycles. There are not many performance differences between the CNN and CatBoost models. Additionally, every statistic is within a good range. Each model works just as well to forecast concrete's CS and STS.

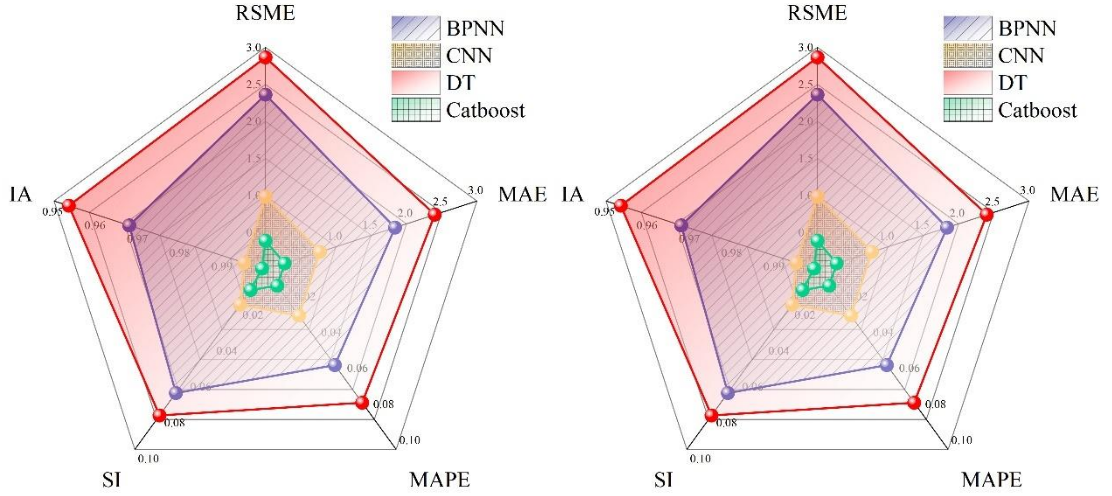

(a) **(b)**

Fig. 15. Evaluation results of predicted values by four models: (a)CS;(b) STS.

A visual comparison of the actual and predicted values of the BPNN, CNN, DT, and CatBoost models on the training and test datasets was carried out further to verify the prediction performance of the proposed ML model. Fig. 16 and Fig. 17 show the correlation between predicted and actual values for CS and STS, indicating that the models have a high capacity for learning the link between input parameters and output. The difference between the predictions of training and test data is also an important consideration when evaluating ML models. In the case of CS, the R^2 values were 0.953 and 0.890 for the BPNN training and test datasets, 0.984 and 0.981 for CNN, 0.838 and 0.838 for DT, and 0.999 and 0.997 for CatBoost. In the case of STS, R^2 was 0.921 and 0.905 for BPNN, 0.984 and 0.980 for CNN, 0.872 and 0.874 for DT, and 0.999 and 0.996 for CatBoost. The DT model had the smallest difference between training and test data predictions but the lowest R^2 value. The CatBoost model's R^2 is nearly equal to 1, and there is not much difference between the test and training data predictions. However, for the BPNN model, the differences between the predictions of training data and that of test data are larger than for the other models. The CNN and CatBoost models show similar correlation results; however, the CNN model's R^2 is lower than the CatBoost model's. Therefore, the CatBoost model performs better than the other models. It should be noted that all models with R^2 values greater than 0.8 show a high degree of reliability in forecasting the RMP of SFMVSSC. The complexity of the data set increases significantly when differences in laboratory settings, apparatus, and MVSS dispersion techniques are considered. Therefore, R^2 values greater than 0.8 can be regarded as reliable results.

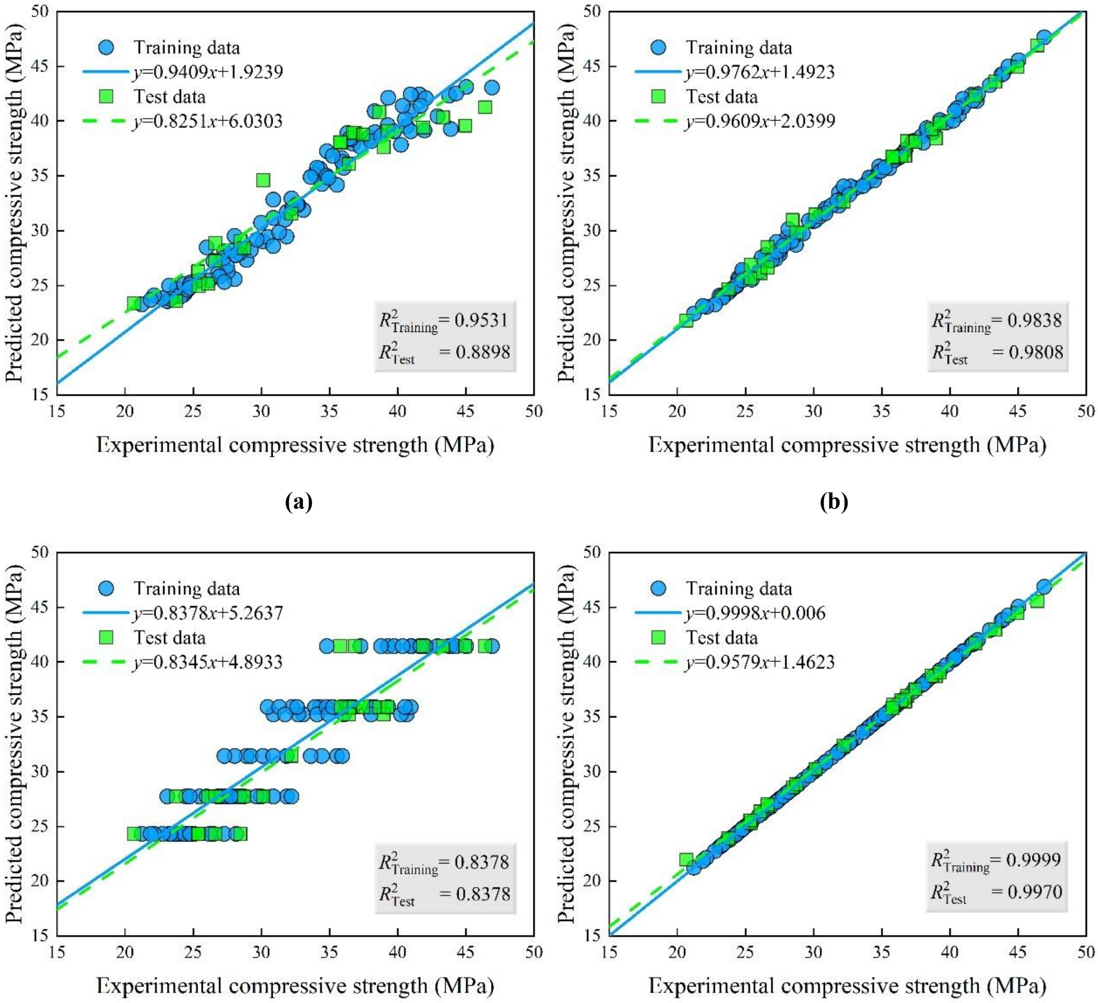

(a) **(b)**

(c) **(d)**

Fig. 16. Correlation between ML predicted and actual values of CS: (a) BPNN; (b) CNN; (c) DT; (d) CatBoost.

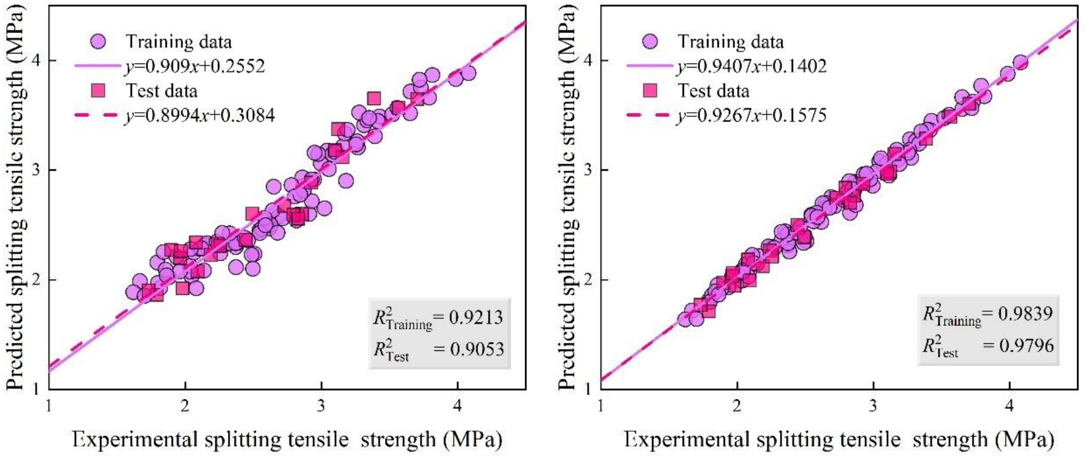

(a) **(b)**

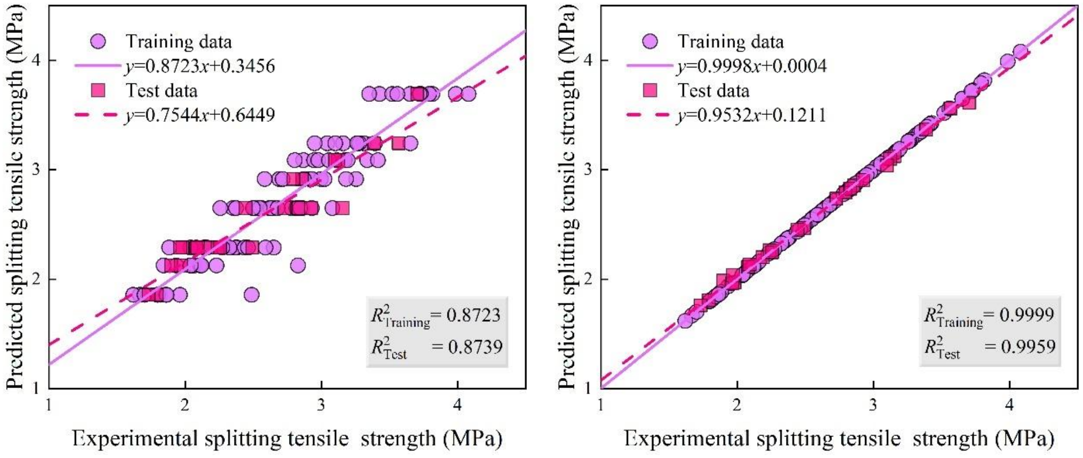

(c) **(d)**

Fig. 17. Correlation between ML predicted and actual values of STS: (a) BPNN; (b) CNN; (c) DT; (d) CatBoost.

5.2 Taylor diagram

The Taylor diagram is one of the most useful methods for assessing the performance of predictive models. The plot illustrates the most reliable and accurate model by comparing its distance from a reference point (the actual value). The model closest to the reference point is considered to be the most accurate model (Band et al., 2021). Fig. 18 demonstrates the performance of multiple ML models in a regression task assessed by Taylor diagrams, where model performance is measured by looking at the SD and correlation of the model's predicted values with the real data. For CS, CatBoost is closest to the reference point (RMSE = 0.391 MPa), with R^2 of 0.999, and the predicted SD is close to the measured value (6.965 vs. 6.712 MPa). For STS, CatBoost is closest to the reference point (RMSE=0.037 MPa), with R^2 of 0.999 and a predicted SD close to the measured value (0.560 vs. 0.591 MPa). Combined with the graphs, it is pointed out that CatBoost is closest to the reference point in the Taylor diagram, indicating that it has the best performance in terms of fitting accuracy, data dispersion and correlation, and has the best overall performance.

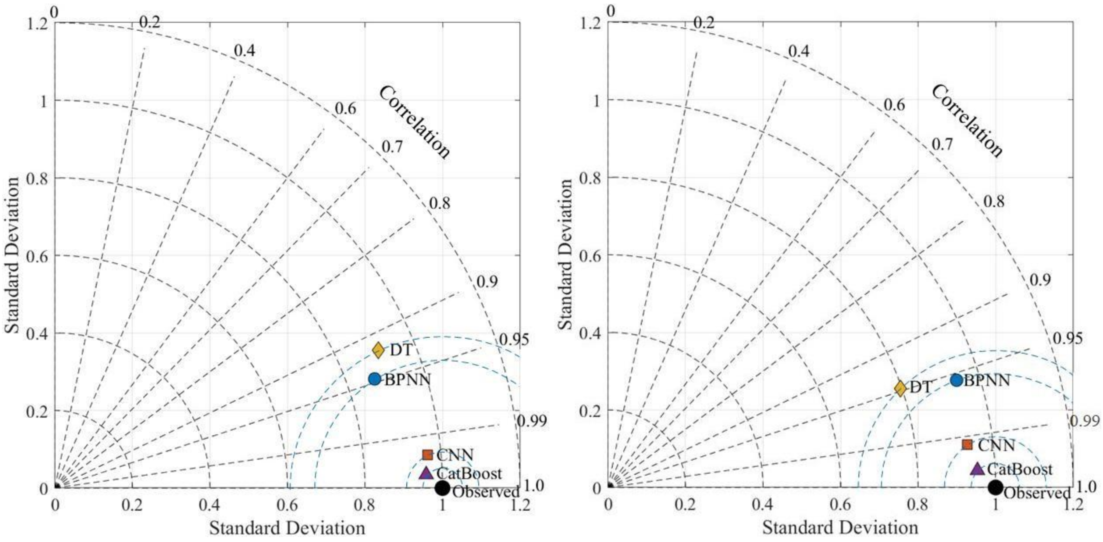

(a) **(b)**

Fig. 18. Taylor diagram of the test by four models: (a)CS;(b) STS.

5.3 Error analysis

To further compare the superiority of the BPNN, CNN, DT and CatBoost predictive models, Fig. 19 summarizes the absolute error between the predicted and actual values of the RMP of

SFMVSSC specimens after the F-T cycles predicted by BPNN, CNN, DT and CatBoost predictive models using a box plot. The box plot is a statistical graph that describes the degree of dispersion of a data set. The interquartile range is represented by a box plot in which the horizontal line indicates the median. The median line of a box plot can reflect the stability of optimization results. The data dispersion in the box plot is measured using IQR, the difference between the upper and lower quartiles. As seen in Fig. 19, the midline of CatBoost is in the middle of the field for both CS and STS, which means that the absolute error between the predicted and actual values of the data generated by CatBoost after training is close to 0. In addition, the IQR of CatBoost is smaller than that of DT, CNN and BPNN, indicating that the BPNN and DT algorithms produce relatively large discretization, the CNN algorithm produces medium discretization, and the CatBoost algorithm produces the smallest discretization. It shows that the CatBoost algorithm is the best of the four ML algorithms regarding accuracy and stability.

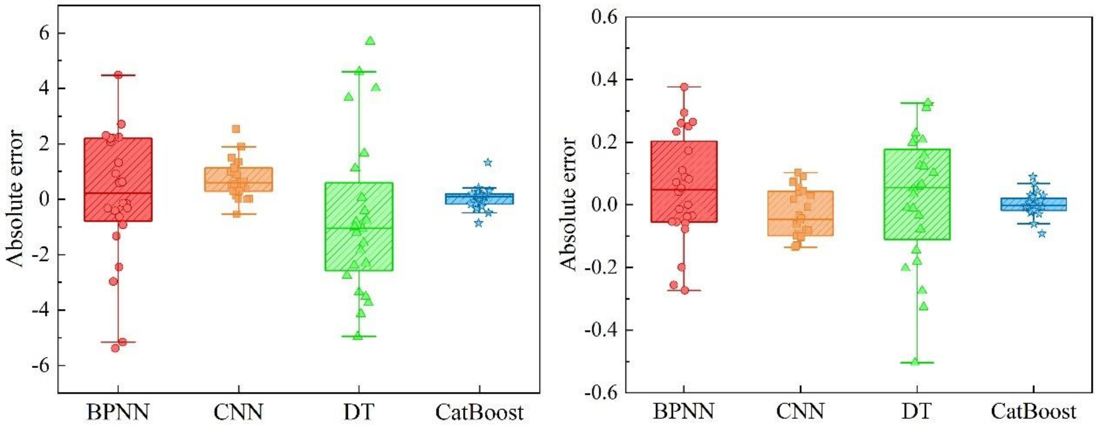

(a) **(b)**

Fig. 19. Absolute errors between predicted and actual values predicted by BPNN, CNN, DT, and CatBoost:(a) Absolute error in CS; (b) Absolute error in STS.

5.4 Monotonicity analysis

In order to apply the developed model more widely, further evaluation is required. Monotonicity analysis is an effective method for assessing the feasibility of the developed model, which uses CS as well as STS and trends between each input variable for comparison with the original database. Table 9 lists the basic settings of the input variables that are reasonable for the monotonicity analysis, corresponding to the mean values of each parameter (see Table 6). Using the basic settings of the predictive model and input variables in Table 9, the relationship between the predicted CS as well as the STS and the input variables being examined can be obtained.

Table 9. Basic setting of input variables for monotonicity analysis.

Parameters	Value
w/c	0.45
RMVSS (%)	50
SFVC (%)	0.75
F-T cycle (times)	100

Fig. 20 shows the variation of predicted CS with w/c, RMVSS, SFVC and F-T cycle respectively. It can be observed that the predicted CS decreases with increasing w/c, RMVSS and F-T cycle and increases with increasing SFVC. This monotonic variation is consistent with the monotonicity of the actual strength of the concrete in Fig. 6, indicating the correctness of the proposed model. The monotonicity analysis of the predicted STS with respect to each input variable is shown in Fig. 21. The trend is similar to the CS and this observation is consistent with the monotonicity of the actual database shown in Fig. 7. Therefore, the consistency of the monotonicity analysis results with the predicted database of STS also validates the correctness of the proposed model.

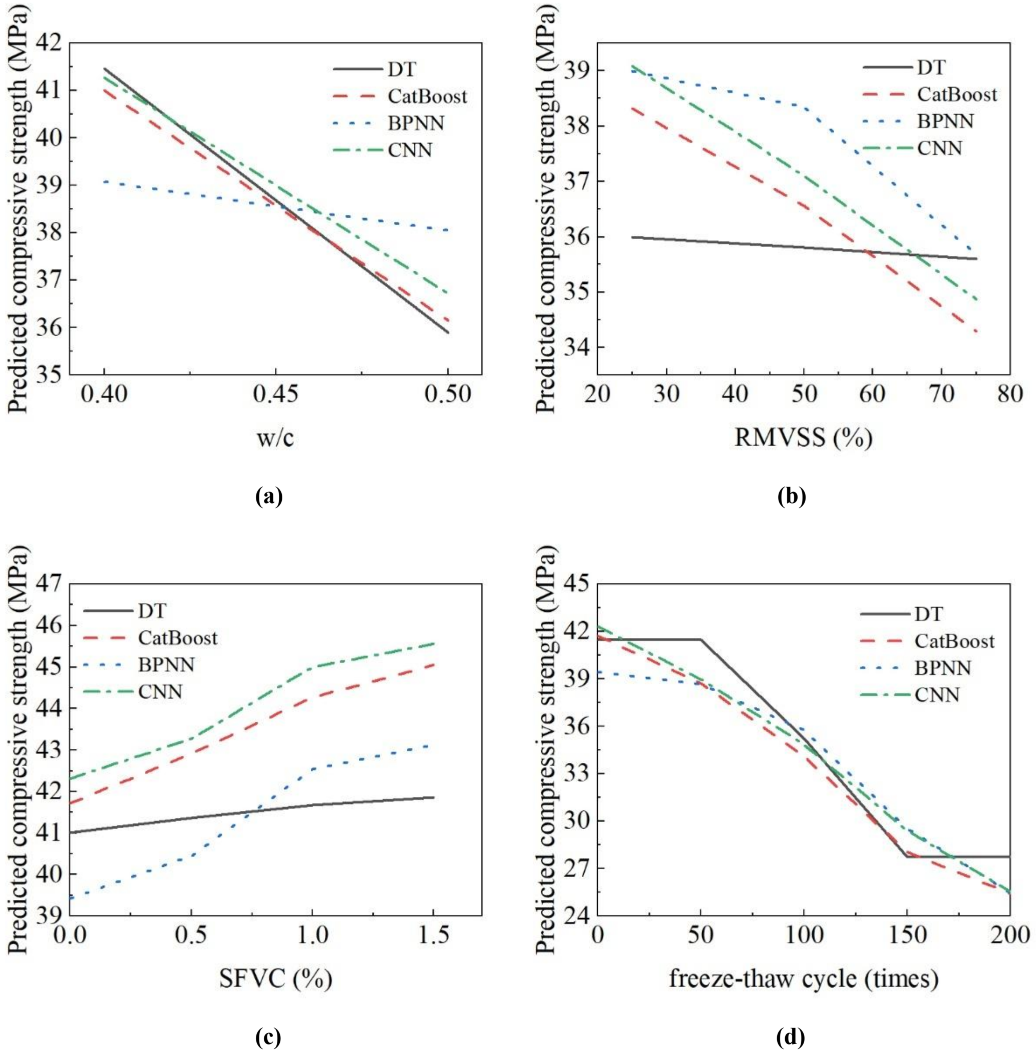

(a) **(b)**

(c) **(d)**

Fig. 20. Monotonicity analysis of the predicted CS versus: (a) w/c; (b) RMVSS; (c) SFVC; (d) F-T cycle.

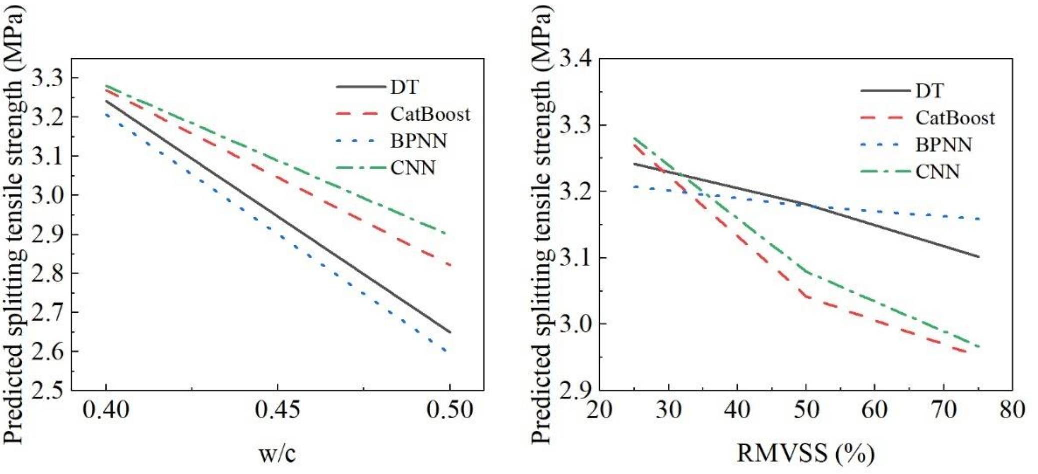

(a) **(b)**

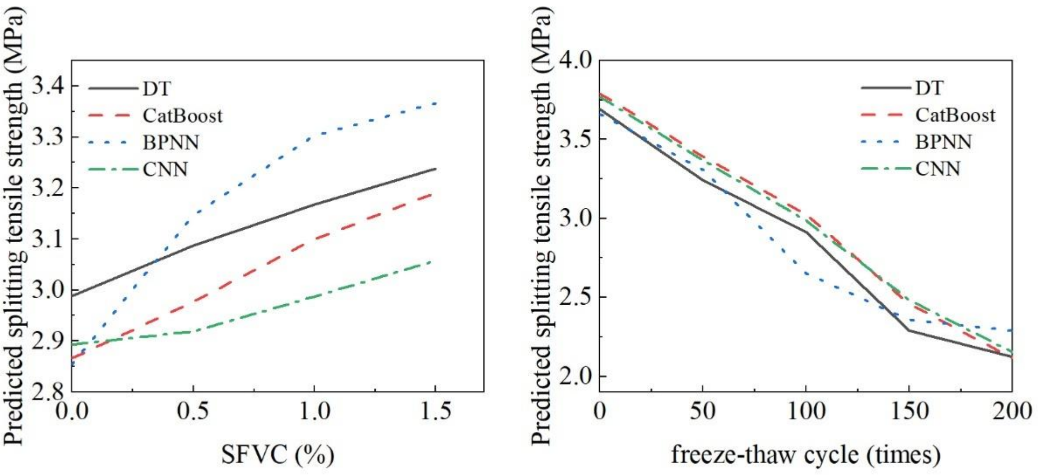

(c) **(d)**

Fig. 21. Monotonicity analysis of the predicted STS versus: (a) w/c; (b) RMVSS; (c) SFVC; (d) F-T cycle.

5.5 Robustness analysis

Robustness analysis were conducted to assess the number of samples with reasonable intensity values as a percentage of the total analysed samples with an appropriate set of input variables. In this way, the robustness analysis further validates the feasibility of the predictive model. To quantify robustness, the robustness ratio is defined as:

$$r = \frac{n_{\text{samples in the reasonable range}}}{n_{\text{total testing samples}}} \tag{12}$$

Where: n is the number.

Based on the original database, these samples were considered reasonable, with predicted CS values ranging from 20.651 MPa to 46.91 MPa and predicted STS values ranging from 1.619 MPa to 4.08 MPa (Table 6). In order to generate the input variables, the four variables are independent of each other according to Fig. 8. Based on the mean and SD of each input variable (as shown in Table 6), the generated samples in which each input variable exceeded its minimum or maximum threshold were removed. Finally, 120 samples were selected for robustness analysis. Fig. 22 and Fig. 23 show the number of samples and the robustness ratios of the four models that lie within a specific range of predicted concrete CS values and STS values, respectively. As can be seen from the figures, using the four models, most of the samples showed predicted CS ranging from 25 MPa to 40 MPa and predicted STS ranging from 2 MPa to 3.5 MPa. In comparison, the robustness ratios of the four models are relatively high, above 99%, and the four models are reliable from the robustness analysis.

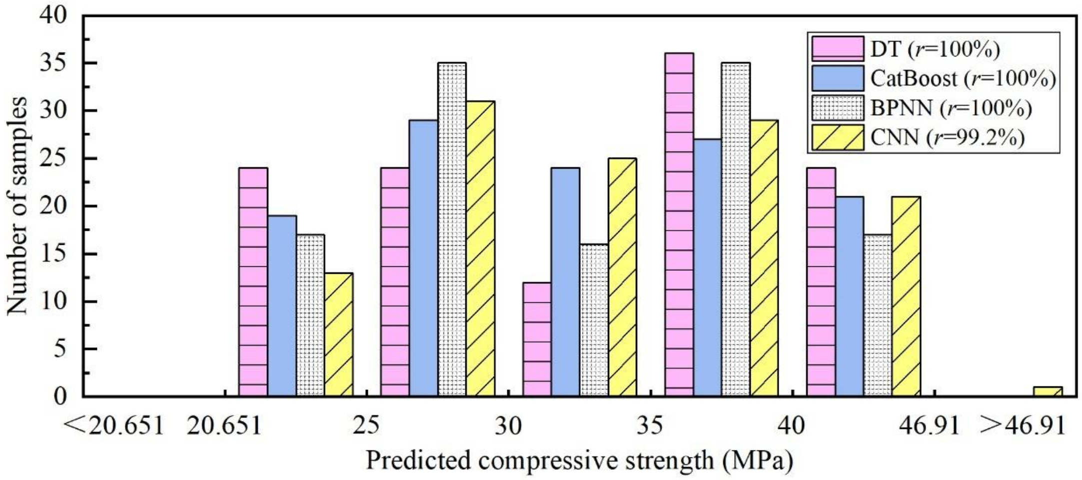

Fig. 22. Robustness analysis of the four proposed models for predicting CS.

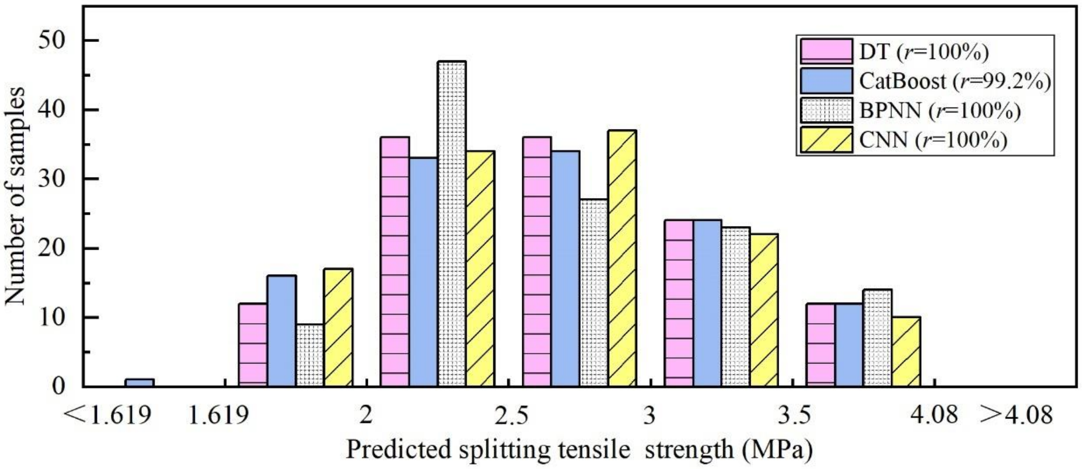

Fig. 23. Robustness analysis of the four proposed models for predicting STS.

5.6 Parametric analysis

This paper uses the CatBoost algorithm to assess the impact of different parameters on the RMP of SFMVSSC since the predictions were satisfactory. The values of several key parameters were entered into the algorithm to predict the strength. The impact of several parameters on the RMP of SFMVSSC was investigated based on the predicted results.

5.6.1 Effect of w/c

Fig. 24 shows the strength response of SFMVSSC as the w/c changes. The strength falls as the w/c increases, the cementitious material decreases after hydration, and the bond between the matrix decreases, causing the strength to decrease. In addition, the internal void ratio of concrete with a high w/c increases, its water retention capacity worsens, the early water is easily dispersed, and the hydration reaction is insufficient.

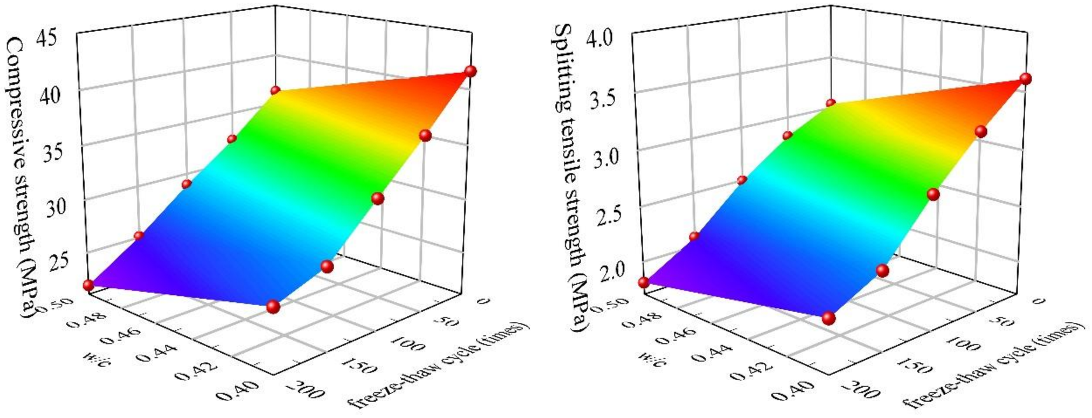

(a) **(b)**

Fig. 24. Effect of variation of w/c on strength of SFMVSSC: (a)CS;(b) STS.

5.6.2 Effect of RMVSS

Fig. 25 shows the strength response of SFMVSSC as the RMVSS changes. The CS and STS of SFMVSSC decreases as the RMVSS increases. At 100 F-T cycles, CS decreased by 4.19 MPa and 3.32 MPa, while STS decreased by 0.25 MPa and 0.08 MPa when the RMVSS increased from 25% to 50% to 75%. Since MVSS aggregate has low strength and a porous structure, increasing RMVSS increases the pores within the concrete, densification becomes poor, and concrete strength ultimately suffers significantly due to the aggregate's total decline in strength. As F-T cycles increase, the downward trend slows down for specimens with high RMVSS, and after 200 F-T cycles, the CS loss is 39.69%, 38.35% and 35.87% for 25%, 50% and 75% RMVSS respectively, and the STS loss is 43.98%, 40.76% and 39.34%, respectively. This is because, as the concrete freezes and thaws process, its internal pores enlarge, the freezing stress in the concrete disperses to the denser pore area, and the frost damage is lessened to enhance the concrete's resistance to frost. This supports the findings of Yuan et al. (Yuan et al., 2023), who previously reported excellent frost resistance in manufactured sand.

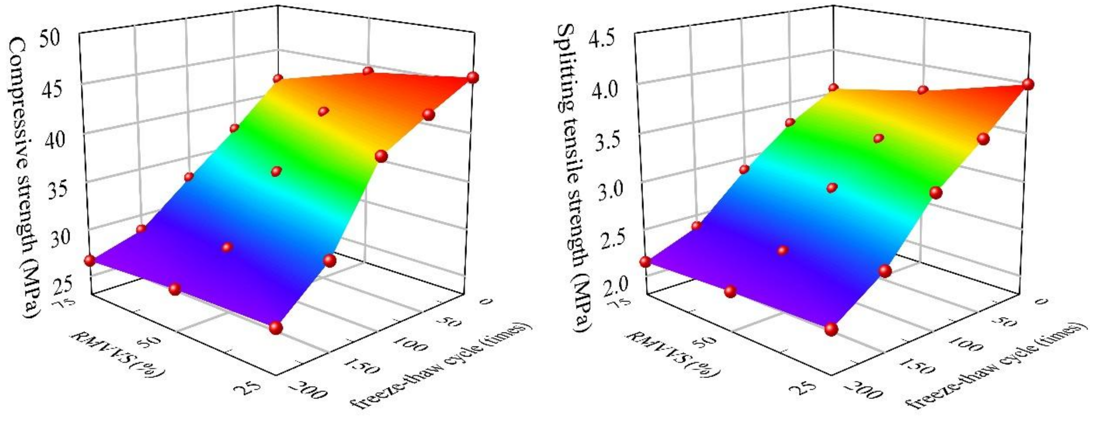

(a) **(b)**

Fig. 25. Effect of variation of RMVSS on strength of SFMVSSC: (a)CS;(b) STS.

5.6.3 Effect of SFVC

Fig. 26 shows the strength response of SFMVSSC as the SFVC changes. With an increase in SFVC, the strength of SFMVSSC exhibits an increasing trend, but the growth gradually slows down.

At 50 F-T cycles, the increase in strength of SFMVSSC is faster with SFVC between 0 and 1%, and the CS increases by 1.14 MPa and the STS by 0.16 MPa, with SFVC between 1% and 1.5%, the strength increase slows down; CS and STS increase by 0.36 MPa and 0.015 MPa, respectively, indicating that the effect on strength decreases with excessive SFVC. As the SFVC increased, the strength of concrete cubes with SF gradually increased and was higher than the corresponding strength of concrete without SF. After 200 F-T cycles, the loss of CS is 41.08%, 38.31%, 35.87% and 34.01% with SFVC of 0%, 0.5%, 1% and 1.5%, respectively, while the loss of STS is 46.17%, 45.02%, 40.35% and 38.28%. Strength loss decreases as SFVC increases, suggesting that SF may enhance MVSSC's ability to withstand F-T cycles. Liang et al. (Liang et al., 2023) also demonstrated SF can strengthen concrete's resilience to F-T. This is because SF can efficiently inhibit and prevent initial crack formation and development in concrete. In addition, the bridging effect can promote microstructure improvement. Macroscopically, mechanical properties and frost resistance can be improved through SF.

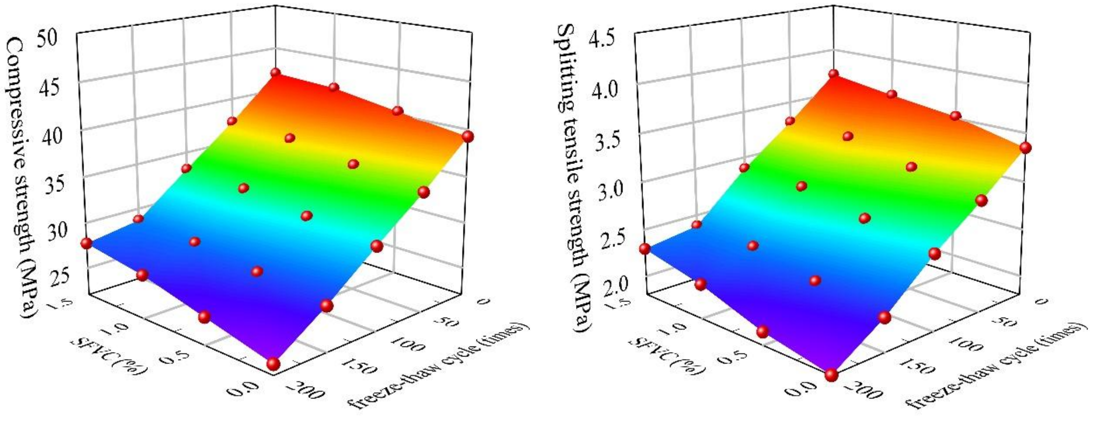

(a) **(b)**

Fig. 26. Effect of variation of SFVC on strength of SFMVSSC: (a)CS;(b) STS.

5.6.4 Effect of F-T cycles

Fig. 27 shows the strength response of SFMVSSC as F-T cycles. As the F-T cycles increased, the specimens' strength steadily declined. For adding 1% SF, when F-T cycles reached 200, the CS and STS of the specimens decreased by 35.87% and 40.35%, respectively. During the test, the F-T cycle easily causes small cracks to form in the concrete, and as the F-T cycles increases, the phenomenon of internal damage, surface cracking and compressive collapse increases; surface spalling leads to the surface density of SFMVSSC, and the material becomes brittle and easy to crush; internal fine pore moisture by freezing expansion pressure, changing the internal hydrostatic pressure, and frost damage and make the concrete internal pore ratio increase, which causes the strength of the concrete to diminish. This is in line with research done by Dong (Dong et al., 2021) and Liang et al. (Liang et al., 2023). The specimens lacking SF had lower strength and resistance to frost, and the CS and STS after 200 F-T cycles reached 23.12 MPa and 1.84 MPa, 41.08% and 44.97% lower than the strength without freezing and thawing, respectively. This demonstrates how applying SF can increase MVSSC's tolerance to F-T.

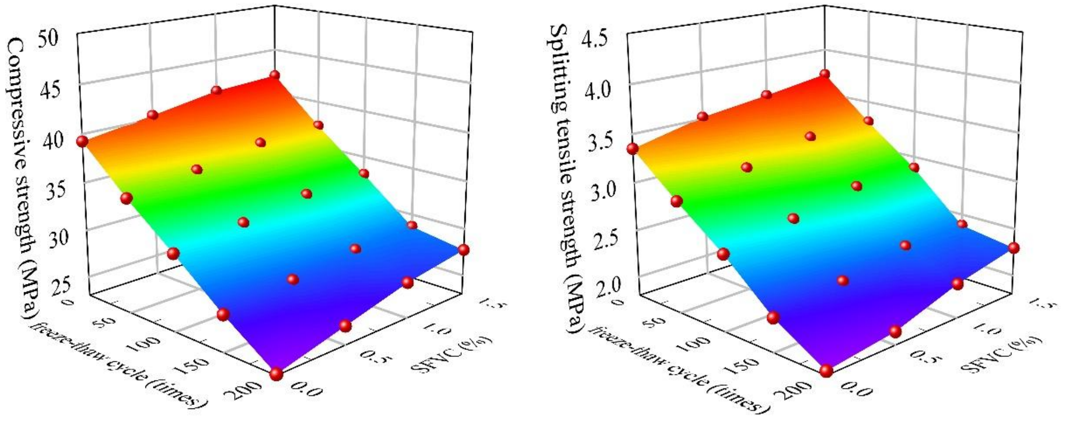

(a) **(b)**

Fig. 27. Effect of F-T cycles variation on SFMVSSC strength: (a)CS;(b) STS.

5.7 Sensitivity analysis

Finally, a sensitivity analysis of SFMVSSC's RMP following a F-T cycle was performed, determining the most crucial input variables using CatBoost. Determine the average degree of change in CatBoost predictions if the value of the feature is changed. The higher the importance rating, the more the anticipated value will vary if the feature is changed. Furthermore, normalization is applied to the feature importance values such that the sum is 100% (Rondinella et al., 2023). Because importance values are always positive, this is possible. Fig. 28 shows the feature importance percentage of the model, it is evident that the F-T cycles have a greater than 65% significance and play the most significant role in forecasting the RMP of the SFMVSSC following the F-T cycle. The w/c, the third percentage of RMVSS, and the smallest influence of SFVC are the next in line.

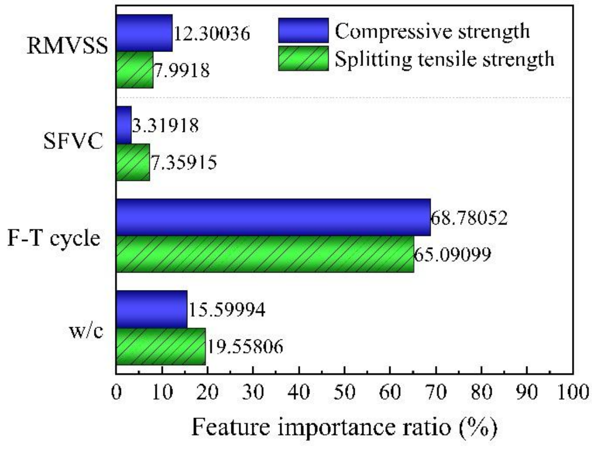

Fig. 28. Feature importance percentage of the model.

5.8 Microstructural Investigation

To study the F-T damage mechanism in SFMVSSC, samples under 0 and 200 F-T cycles were chosen for SEM analysis to analyze the microscopic morphology of the samples, as shown in Fig. 29. During the scanning process, a charging effect occurs when the scanned sample is taken, resulting in a sample discharge during SME imaging. There are interfacial transition zones (ITZ) between the coarse aggregate and the mortar, which is the weak point in the concrete. The organization of the aggregate and cement paste is complete, solid, and free of microcracks, as illustrated in Fig. 29, and the mortar of the MVSSC is securely attached to the aggregate before the

F-T cycle. The ITZ shows visible pores and fissures of different diameters following F-T cycles. The closed pores of MVSSC have a strong pressure relief effect to improve the freeze-up stress of concrete and disperse the large stagnant air bubbles into the small unconnected pores, resulting in the improvement of the structure of the ITZ to increase concrete's resistance to freezing. After the F-T cycle in Fig. 29(d), SF strengthens the concrete's internal structure, minimizes pores and cracks, and forms a good ITZ between the SF and the cement paste on both sides of the pores, which can effectively bridge the micro-cracks caused by the F-T cycle and thus improve freeze resistance of MVSSC.

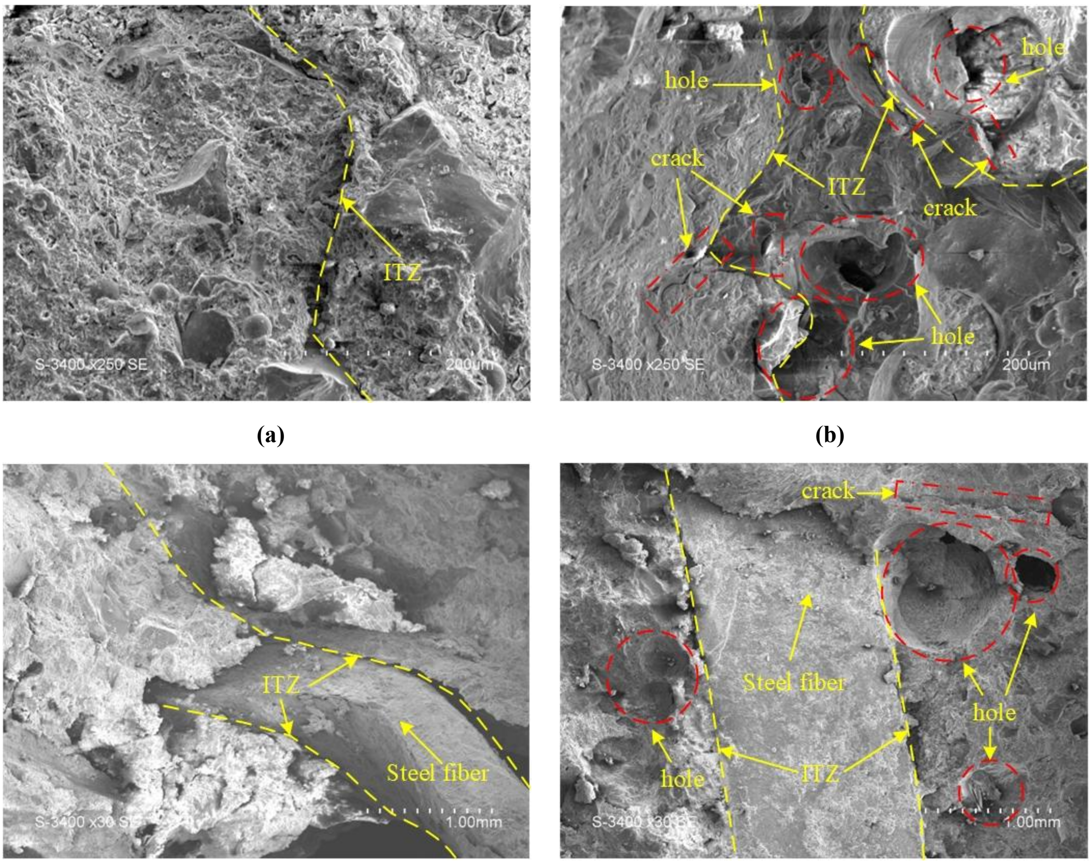

(a) **(b)**

(c) **(d)**

Fig. 29. SME: (a) Aggregate to slurry (0 F-T cycles); (b) Aggregate to slurry (200 F-T cycles) (c) Steel fiber to slurry (0 F-T cycles); (d) Steel fiber to slurry (200 F-T cycles)

6. Conclusions

This work used four ML models to predict the RMP of SFMVSSC after F-T cycles: BPNN, CNN, DT, and CatBoost. Every data utilized came from experiments. Every computer model demonstrated satisfactory predictive performance compared to experimental values and model projections. It was shown that it was possible to forecast the RMP of SFMVSSC after F-T cycles using ML approaches. The computational results' primary finding is that the CatBoost model outperforms the other models. The following are the study's primary findings:

1、 MVSS is suitable for concrete production as a fine aggregate that partially replaces NS. Despite its lower strength, MVSSC meets standards. Its selection as a substitute building material is influenced by its accessibility in the area. Compared with NS, it helps save energy and costs, complies with the strategy of green concrete production, expands the choice of raw materials for concrete, and provides a new direction for the sustainable construction industry.

2、 Breaking through the traditional methods, four ML models (BPNN, CNN, DT, and CatBoost) were presented, and the prediction models were built on a large amount of experimental data to take full advantage of ML technology. The feasibility of each model was evaluated in terms of R^2, RMSE, MAE, MAPE, SI, and IA. It showed that each model could efficiently predict the RMP of SFMVSSC after F-T cycles. All of them have a high level of reliability, which opens a new avenue for predicting the RMP of concrete.

3、 In the comparative analysis of the four ML models, the superior performance of the CatBoost model in predicting the RMP of SFMVSSC after F-T cycles was identified. It exhibits the lowest values of RMSE, MAE, MAPE, and SI, the highest value of IA, and the R^2 closest to 1, demonstrating strong generalizability and accuracy, providing an effective and low-cost new tool for studying the mechanical properties of lightweight aggregate concrete after F-T cycles and filling the gap in the application of this type of model to predict the properties of this type of concrete in the past.

4、 The CatBoost model with the best performance showed an inverse trend of w/c, RMVSS, F-T cycles with concrete strength, and a positive correlation between SFVC and concrete strength. After 200 F-T cycles, the loss of concrete strength decreased as RMVSS increased, and the concrete strength increased as the amount of SFVC increased. Both MVSS and SF can improve the resistance of concrete to frost.

5、 Feature importance analysis shows that F-T cycles are the most important parameter in determining the CS and STS of SFMVSSC, with the importance of both exceeding 65%, which provides clear guidance for focusing and controlling the key factors in further research and engineering practice, and modifies the lack of accurate and quantitative analysis of the importance of each factor in the past.

6、 SF and MVSS can increase concrete's resistance to freezing temperatures by investigating the SFMVSSC's F-T damage mechanism through microanalysis. The most practical SFVC to increase concrete's resistance to frost is 1% SF, which provides microscopic theoretical support for optimizing the concrete proportion design and helps further improve concrete performance in cold regions.

Data Availability

Upon a reasonable request, the corresponding author will make part or all of the models, codes, or data used to support the study's findings available.

Declaration of Competing Interest

According to the authors, the study presented in this paper is independent of any known financial or personal relationships.

Declaration of funding

This research was financially supported by the Jilin Provincial Science and Technology Development Plan Project (20250203145SF). The sponsors are much appreciated by the authors. However, the views, discoveries, recommendations, and opinions shared by the authors in this work are wholly their own and might not reflect those of the sponsors.

References

Alarfaj, M., Qureshi, H. J., Shahab, M. Z., Javed, M. F., Arifuzzaman, M., & Gamil, Y. (2024). Machine learning based prediction models for spilt tensile strength of fiber reinforced recycled aggregate concrete. *Case Studies in Construction Materials, **20***. https://doi.org/10.1016/j.cscm.2023.e02836

Alyaseen, A., Poddar, A., Kumar, N., Sihag, P., Lee, D., kumar, R., & Singh, T. (2024). Assessing the compressive and splitting tensile strength of self-compacting recycled coarse aggregate concrete using machine learning and statistical techniques. *Materials Today Communications, **38***. https://doi.org/10.1016/j.mtcomm.2023.107970

ASTM. (2016). C1723-16: Standard guide for examination of hardened concrete using scanning electron microscopy. ASTM International West Conshohocken, PA, USA.

Bai, J., Zhao, Y., Shi, J., & He, X. (2022). Damage degradation model of aeolian sand concrete under freeze–thaw cycles based on macro-microscopic perspective. *Construction and Building Materials, **327***. https://doi.org/10.1016/j.conbuildmat.2022.126885

Band, S. S., Heggy, E., Bateni, S. M., Karami, H., Rabiee, M., Samadianfard, S., Chau, K. W., & Mosavi, A. (2021). Groundwater level prediction in arid areas using wavelet analysis and Gaussian process regression. *Engineering Applications of Computational Fluid Mechanics, 15(1),* 1147-1158. https://doi.org/10.1080/19942060.2021.1944913

Benahsina A., El Haloui Y., Taha Y., Elomari M. & Bennouna M. Abdouh. (2022). Natural sand substitution by copper mine waste rocks for concrete manufacturing. *Journal of Building Engineering, **47***. https://doi.org/10.1016/j.jobe.2021.103817

Bouras, Y., & Li, L. (2023). Utilisation of Machine Learning Techniques to Model Creep Behaviour of Low-Carbon Concretes. *Buildings, **13(9)***. https://doi.org/10.3390/buildings13092252

CABR (China Academy of Building Research). (2002). JGJ51-2002: Light Aggregate Concrete Technical Specification. CABR, China.

CABR (China Academy of Building Research). (2009). GB/T 50082-2009: Standard for test methods of long-term performance and durability of ordinary concrete. CABR, China.

CABR (China Academy of Building Research). (2019). GB/T 50081-2019: Standard for test methods of concrete physical and mechanical properties. CABR, China.

Cai, B., Hu, W.-L., & Fu, F. (2021). Numerical Analysis of Seismic Performances of Post-Fire Scoria Aggregate Concrete Beam-Column Joints. *Fire, **4(4)***. https://doi.org/10.3390/fire4040070

Cai, B., Lin, X., Fu, F., & Wang, L. (2022). Postfire residual capacity of steel fiber reinforced volcanic scoria concrete using PSO-BPNN machine learning. *Structures, **44**,* 236-247. https://doi.org/10.1016/j.istruc.2022.08.012

Candice, B., Anna, C., & Gonzalo, M. M. (2020). A comparative analysis of gradient boosting algorithms. *Artificial Intelligence Review (prepublish)*,1-31.

Chang, W., Wang, X., Yang, J., & Qin, T. (2023). An Improved CatBoost-Based Classification Model for Ecological Suitability of Blueberries. *Sensors, **23(4)***. https://doi.org/10.3390/s23041811

Dong, F., Wang, H., Yu, J., Liu, K., Guo, Z., Duan, X., & Qiong, X. (2021). Effect of freeze–thaw cycling on mechanical properties of polyethylene fiber and steel fiber reinforced concrete. *Construction and Building Materials, **295***. https://doi.org/10.1016/j.conbuildmat.2021.123427

El-Nadoury W.W. (2021). Production of sustainable concrete using sawdust. *Magazine of Civil Engineering, **(105)**,* 10507-10507. https://doi.org/10.34910/MCE.105.7

Huang, Y., Dong, L., Qi, X., Wang, T., Li, P., & Zhong, J. (2023). Effects of mix components on mechanical properties of marine volcanic-scoria concrete under axial compression. *Case Studies in Construction Materials, **18***. https://doi.org/10.1016/j.cscm.2023.e01837

Hussain, F., Ali Khan, S., Khushnood, R. A., Hamza, A., & Rehman, F. (2022). Machine Learning-Based Predictive Modeling of Sustainable Lightweight Aggregate Concrete. *Sustainability, **15(1)***. https://doi.org/10.3390/su15010641

Kang, J., Chen, X., & Yu, Z. (2023). Effect of polypropylene fiber on frost resistance and carbonation resistance of manufactured sand concrete. *Structures, **56***. https://doi.org/10.1016/j.istruc.2023.104896.

Karahan, O., & Atis, C. D. (2011). The durability properties of polypropylene fiber reinforced fly ash concrete. *Materials and Design, **32(2)**,* 1044-1049. https://doi.org/10.1016/j.matdes.2010.07.011

Kioumarsi, M., Dabiri, H., Kandiri, A., & Farhangi, V. (2023). Compressive strength of concrete containing furnace blast slag; optimized machine learning-based models. *Cleaner Engineering and Technology, **13***. https://doi.org/10.1016/j.clet.2023.100604

Laouissi, A., Blaoui, M. M., Abderazek, H., Nouioua, M., & Bouchoucha, A. (2022). Heat treatment process study and ANN-GA based multi-response optimization of C45 steel mechanical properties. *Metals and Materials International, 28(12),* 3087-3105. https://doi.org/10.1007/s12540-022-01197-6

Li, J., Huang, J., Niu, J., & Wan, C. (2019). Mesoscopic study on axial compressive damage of steel fiber reinforced lightweight aggregate concrete. *Construction and Building Materials, **196**,* 14-25. https://doi.org/10.1016/j.conbuildmat.2018.11.135

Li, Y., Gu, Z., Zhao, B., Zhang, J., & Zou, X. (2022). Experimental Study on Mechanical Properties of Basalt Fiber Concrete after Cryogenic Freeze−Thaw Cycles. *Polymers, **15(1)***. https://doi.org/10.3390/polym15010196

Liang, G., Yao, W., & Wei, Y. (2023). A green ultra-high performance geopolymer concrete containing recycled fine aggregate: Mechanical properties, freeze-thaw resistance and microstructure. *Science of The Total Environment, **895***. https://doi.org/10.1016/j.scitotenv.2023.165090

Liao, X., Yan, Q., Su, L., Qiu, Y., Ren, J., & Zhang, C. (2024). Automatic assessment of freeze-thaw damage in concrete structures using piezoelectric-based active sensing approach and deep learning technique. *Engineering Structures, **302***. https://doi.org/10.1016/j.engstruct.2024.117453

Liu, K., Zou, C., Zhang, X., & Yan, J. (2021). Innovative prediction models for the frost durability of recycled aggregate concrete using soft computing methods. *Journal of Building Engineering, **34***. https://doi.org/10.1016/j.jobe.2020.101822

Luo, X., Xing, G., Qiao, L., Miao, P., Yu, X., & Ma, K. (2023). Multi-objective optimization of the mix proportion for dune sand concrete based on response surface methodology. *Construction and Building Materials, **366***. https://doi.org/10.1016/j.conbuildmat.2022.129928

Maherian, M. F., Baran, S., Bicakci, S. N., Toreyin, B. U., & Atahan, H. N. (2023). Machine learning-based compressive strength estimation in nano silica-modified concrete. *Construction and Building Materials, **408***. https://doi.org/10.1016/j.conbuildmat.2023.133684

Mahmoudian, A., Tajik, N., Taleshi, M. M., Shakiba, M., & Yekrangnia, M. (2023). Ensemble machine learning-based approach with genetic algorithm optimization for predicting bond strength and failure mode in concrete-GFRP mat anchorage interface. *Structures, 57*. https://doi.org/10.1016/j.istruc.2023.105173

Morsy, A. M., Abd Elmoaty, M., & Harraz, A. B. (2022). Predicting mechanical properties of engineering cementitious composite reinforced with PVA using artificial neural network. *Case Studies in Construction Materials, 16,* e00998. https://doi.org/10.1016/j.cscm.2022.e00998

Pal, A., Ahmed, K. S., Hossain, F. M. Z., & Alam, M. S. (2023). Machine learning models for predicting compressive strength of fiber-reinforced concrete containing waste rubber and recycled aggregate. *Journal of Cleaner Production, **423***. https://doi.org/10.1016/j.jclepro.2023.138673

Quan, T. V., Quoc, D. V., & Si, H. L. (2022). Evaluating compressive strength of concrete made with recycled concrete aggregates using machine learning approach. *Construction and Building Materials, **323***. https://doi.org/10.1016/j.conbuildmat.2022.126578

RodrÃ-guez-SÃ¡nchez, A. E., Plascencia-Mora, H., & Acevedo-Alvarado, M. (2024). Neural network-driven interpretability analysis for evaluating compressive stress in polymer foams. *Journal of Cellular Plastics, 60(4),* 237-258. https://doi.org/10.1177/0021955X241255102

Rondinella, F., Daneluz, F., Hofko, B., & Baldo, N. (2023). Improved predictions of asphalt concretes’ dynamic modulus and phase angle using decision-tree based categorical boosting model. *Construction and Building Materials, **400***. https://doi.org/10.1016/j.conbuildmat.2023.132709

Sun, B., Ding, L., Ye, G., & De Schutter, G. (2023). Mechanical properties prediction of blast furnace slag and fly ash-based alkali-activated concrete by machine learning methods. *Construction and Building Materials, **409***. https://doi.org/10.1016/j.conbuildmat.2023.133933

Tang, H., Yang, Y., Li, H., Xiao, L., & Ge, Y. (2023). Effects of chloride salt erosion and freeze–thaw cycle on interface shear behavior between ordinary concrete and self-compacting concrete. *Structures,**56***. https://doi.org/10.1016/j.istruc.2023.104990

Tchamdjou, W. H. J., Cherradi, T., Abidi, M. L., & Pereira-de-Oliveira, L. A. (2017). The use of volcanic scoria from ‘Djoungo’ (Cameroon) as cement replacement and fine aggregate by sand substitution in mortar for masonry. *European Journal of Environmental and Civil Engineering, **24(1)***, 60-78. https://doi.org/10.1080/19648189.2017.1364298

Tchamdjou, W. H. J., Grigoletto, S., Michel, F., Courard, L., Abidi, M. L., & Cherradi, T. (2017). An investigation on the use of coarse volcanic scoria as sand in Portland cement mortar. *Case Studies in Construction Materials, 7,* 191-206. https://doi.org/10.1016/j.cscm.2017.07.005

Thai, D.-K., Le, D.-N., Hoan Doan, Q., Pham, T.-H., & Nguyen, D.-N. (2023). Classification models for impact damage of fiber reinforced concrete panels using Tree-based learning algorithms. *Structures, **53**,* 119-131. https://doi.org/10.1016/j.istruc.2023.04.062

Vadavalli, A., & Radhakrishnan, S. (2020). Bagging and Boosting Ensembles for Conflict Resolution on Heterogeneous Data, in: P. Vasant, I. Zelinka, G.W. Weber (Eds.). *Intelligent Computing and Optimization, Springer International Publishing, Cham,430-445*. https://doi.org/10.1007/978-3-030-68154-8.

Warati, Darwish, Feyessa, & Ghebrab. (2019). Suitability of Scoria as Fine Aggregate and Its Effect on the Properties of Concrete. *Sustainability, **11(17)***. https://doi.org/10.3390/su11174647

Xiao, Q., Hao, S., Ning, X., & Liang, Y. (2018). Review on the influence of fiber on frost resistance durability of concrete. *Concrete, **6**,* 68-71.

Yang, D., Bin, L., Li, W., Xia, J., & Zhou, Y. (2017). Domestic and Overseas Research and Utilization on Lightweight Aggregate Concrete Prepared with Scoria. *The World of Building Materials,* **38,** 26-30.

Yang, S., Sun, J., & Zhifeng, X. (2024). Prediction on compressive strength of recycled aggregate self-compacting concrete by machine learning method. *Journal of Building Engineering, **88***. https://doi.org/10.1016/j.jobe.2024.109055

Yu, Y., Liang, S., Samali, B., Nguyen, T. N., Zhai, C., Li, J., & Xie, X. (2022). Torsional capacity evaluation of RC beams using an improved bird swarm algorithm optimised 2D convolutional neural network. *Engineering Structures, **273***. https://doi.org/10.1016/j.engstruct.2022.115066

Yuan, C., Xu, S., Wang, Y., & Yang, B. (2023). Research on frost resistance durability and mechanism of machine-made sand UHPC. *Concrete, **9***.

Zhang, C., &Ma, Y. (2012). Ensemble machine learning: Methods and applications. https://doi.org/10.1007/978-1-4419-9326-7.

Zhang, H., Chen, M., Bai, S., & Cai, Q. (2015). Experimental research on compressive and tensile properties of the concrete reinforced with layered hybrid fiber. *Journal of Water Resources and Architectural Engineering, **13(5)**,* 131-135.

Zhang, H., Ji, S. S., Liu, H., Liu, X. Y., Li, X. C., Zheng, S. Z., & Cao, Z. X. (2024). Research on dynamic splitting tensile damage characteristics of steel fiber reinforced concrete under freeze-thaw cycle environment based on AE. *Journal of Building Engineering, **84***. https://doi.org/10.1016/j.jobe.2024.108490

Zhang, J., Huang, Y., Wang, Y., & Ma, G. (2020). Multi-objective optimization of concrete mixture proportions using machine learning and metaheuristic algorithms. *Construction and Building Materials, **253***. https://doi.org/10.1016/j.conbuildmat.2020.119208

Zhou, Y., Liu, X., Xing, F., Cui, H., & Sui, L. (2016). Axial compressive behavior of FRP-confined lightweight aggregate concrete: An experimental study and stress-strain relation model. *Construction and Building Materials, **119**,* 1-15. https://doi.org/10.1016/j.conbuildmat.2016.02.180